JEM Journal of Experimental Medicine

ARTICLE

Ferrous iron–activatable drug conjugate achieves potent MAPK blockade in *KRAS*-driven tumors

Honglin Jiang[1,2], Ryan K. Muir[3], Ryan L. Gonciarz[3], Adam B. Olshen[2,4], Iwei Yeh[2,5], Byron C. Hann[2], Ning Zhao[6], Yung-hua Wang[6], Spencer C. Behr[6], James E. Korkola[7], Michael J. Evans[2,6], Eric A. Collisson[1,2], and Adam R. Renslo[2,3]

KRAS mutations drive a quarter of cancer mortality, and most are undruggable. Several inhibitors of the MAPK pathway are FDA approved but poorly tolerated at the doses needed to adequately extinguish RAS/RAF/MAPK signaling in the tumor cell. We found that oncogenic *KRAS* signaling induced ferrous iron (Fe^{2+}) accumulation early in and throughout mutant *KRAS*-mediated transformation. We converted an FDA-approved MEK inhibitor into a ferrous iron–activatable drug conjugate (FeADC) and achieved potent MAPK blockade in tumor cells while sparing normal tissues. This innovation allowed sustainable, effective treatment of tumor-bearing animals, with tumor-selective drug activation, producing superior systemic tolerability. Ferrous iron accumulation is an exploitable feature of *KRAS* transformation, and FeADCs hold promise for improving the treatment of *KRAS*-driven solid tumors.

Introduction

The uptake, transport, and storage of essential divalent metals such as iron and copper are tightly controlled in biology but often dysregulated in cancer (Chang, 2015). Transcriptional profiling has revealed links between elevated iron levels and poor prognosis in gliomas (Han et al., 2018), breast cancer (Torti and Torti, 2013a), and prostate cancer (Tesfay et al., 2015), but clinical studies based on iron chelation have failed (Buss et al., 2003). New appreciation for the crucial importance of iron homeostasis has been revealed through genome-wide association studies and the use of a new small-molecule iron probes with oxidation-state specificity (Aron et al., 2018; Bruemmer et al., 2020; Chang, 2015; Hirayama, 2019). Indeed, a recent functional screen found that the single indispensable function of the lysosome in cell proliferation was the pH-dependent unloading, reduction, and delivery of bioavailable Fe^{2+} to the cell (Weber et al., 2020). Intriguingly, elevated Fe^{2+} is linked by an unknown mechanism to a drug-tolerant cancer cell state (Hangauer et al., 2017) that is also highly susceptible to ferroptosis (Dixon and Stockwell, 2014; Stockwell et al., 2017). Taken together, these studies suggest that access to bioavailable Fe^{2+} (as opposed to total iron) is an important factor in cancer cell survival and proliferation. On the other hand, a role for copper in signaling through MEK1 has been proposed, with reduced bioavailability of Cu decreasing MEK kinase activity and oncogenic *BRAF*-driven tumorigenesis (Brady et al., 2014). Conversely, oncogenic $BRAF^{V600E}$ and $KRAS^{G12D}$ mutations lead to a decreased intracellular labile Cu(I) pool (Chung et al., 2019). Despite these new insights into altered metal ion homeostasis and cancer biology, therapeutic approaches that aimed at exploiting such changes have been slow to emerge.

Pancreatic ductal adenocarcinoma (PDA) is among the most aggressive and lethal solid tumors with a 5-yr survival rate of ∼9% (Siegel et al., 2018). Systemic therapies are only marginally effective in this disease, and no targeted therapies against somatic aberrations are currently available. *KRAS* mutation is a cardinal feature of PDA. Constitutive RAS activation drives uncontrolled proliferation and enhances the survival of cancer cells and also sensitizes tumor cells to ferroptosis (Dixon et al., 2012). Here, we explore the elevation of intracellular Fe^{2+} in mutant *KRAS*-driven tumor cells in vitro and in vivo and target these tumors with a prototypical ferrous iron–activatable drug conjugate (FeADC) that ablates MAPK signaling in tumor while sparing tissues that are dependent on physiologic RAS–MAPK signaling for tissue homeostasis, which allows a dramatically improved therapeutic window.

[1]Division of Hematology and Oncology, Department of Medicine, University of California, San Francisco, San Francisco, CA; [2]Helen Diller Family Comprehensive Cancer Center, University of California, San Francisco, San Francisco, CA; [3]Department of Pharmaceutical Chemistry, University of California, San Francisco, San Francisco, CA; [4]Department of Epidemiology and Biostatistics, University of California, San Francisco, San Francisco, CA; [5]Departments of Pathology and Dermatology, University of California, San Francisco, San Francisco, CA; [6]Department of Radiology and Biomedical Imaging, University of California, San Francisco, San Francisco, CA; [7]Center for Spatial Systems Biomedicine, Oregon Health & Sciences University, Portland, OR.

Correspondence to Eric A. Collisson: collissonlab@gmail.com; Adam R. Renslo: adam.renslo@ucsf.edu.

Results

A ferrous iron signature is prognostic in pancreatic adenocarcinoma

To evaluate tumor iron metabolism in an unbiased manner, we first evaluated mRNA transcriptional data from 23 tumor types profiled by The Cancer Genome Atlas (TCGA) with a focus on iron homeostatic programs using biological pathway activity method (Ding et al., 2019). The cancer types with the highest Z-scores for iron metabolism were all RAS–MAPK pathway-driven malignancies, which include glioblastoma multiforme, lung adenocarcinoma, and PDA (PAAD; Fig. 1 A). *STEAP3* (a lysosomal ferrireductase) and *TFRC* (transferrin receptor) encode key genes in iron homeostasis. We compared levels of *STEAP3* and *TFRC* mRNA to overall patient survival (OS) in PDA, a disease with the highest rate of *KRAS* mutation. Both *STEAP3* and *TFRC* expression are associated with shorter OS by Cox regression analysis (Fig. 1 B). Liver metastasis is a uniformly poor prognostic feature in PDA. We examined *STEAP3* expression in an independent primary and metastatic PDA dataset (Aguirre et al., 2018) and found *STEAP3* expression to be higher in liver metastases than in all other metastatic sites ($P = 0.0001$; Fig. 1 C). Gallium-68 citrate is a clinically studied radiotracer that mimics (Fe^{3+}-loaded) holotransferrin and can quantify iron demand in cancer patients (Behr et al., 2018; Larson et al., 1980). To assess iron avidity in PDA, we conducted an exploratory human imaging study with Ga-68 citrate positron emission tomography (PET) in our PDA patients. Quantitative analysis of the imaging data showed that visceral and bony PDA metastases were highly avid for Gallium-68 compared to normal tissues, which is consistent with an iron avid phenotype in PDA (Fig. 1 D).

We next measured avidity for Fe^{3+} and Fe^{2+} in xenograft mouse models, to better understand our clinical observations. We observed enhanced uptake of Gallium-68 in oncogenic *KRAS*-driven PDA xenografts as compared to breast cancer xenografts with wild-type *KRAS* (Fig. 1 E). To assess levels of ferrous iron (Fe^{2+}) in the same tumors, we used ^{18}F-TRX, our recently described radiotracer designed specifically to detect Fe^{2+} (Muir et al., 2019; Zhao et al., 2021). We found that oncogenic *KRAS*-driven PDA tumors (as compared to the *KRAS* wild-type breast cancer examined) were enriched in Fe^{2+}, which mirrors the findings with ^{68}Ga (Fig. S1 A). Together, these findings suggest that increased iron uptake and its reduction to the labile ferrous form is a common feature of PDA and is associated with poor prognosis in patients.

Oncogenic *KRAS* drives accumulation of labile ferrous iron

We next investigated the mechanism(s) by which oncogenic *KRAS* drives Fe^{2+} accumulation. To temporally control $Kras^{G12D}$ expression in primary cells, we isolated primary dermal fibroblasts from a novel Lox–Stop–Lox *Kras* (*LSL-Kras*^{G12D}) conditional mouse model, in which high expression of $Kras^{G12D}$ is initiated by the removal of a Cre recombinase-sensitive transcriptional stop element. We activated the *LSL-Kras*^{G12D} allele with adenovirus-expressing Cre recombinase (AdCre). We collected protein from primary fibroblasts at 24, 48, and 72 h after AdCre infection and observed robust expression of $Kras^{G12D}$ protein and also increased MAPK signaling, as demonstrated by phospho-ERK induction (Fig. 2 A). Intracellular labile Fe^{2+} also increased, as measured with the Fe^{2+}-selective fluorescent dye SiRhoNox (Aron et al., 2018; Hirayama et al., 2019; Hirayama et al., 2017; Fig. 2, B and C). Proliferation slowed upon $Kras^{G12D}$ expression and $p21^{CIP}$ levels increased, which is consistent with oncogene-induced senescence (Serrano et al., 1997; Fig. S1, B and C). We also isolated primary pancreatic ductal cells (Reichert et al., 2013) from Lox–Stop–Lox *Kras* (*Kras*$^{LSL\_G12D}$); *Trp53*$^{flox/flox}$ animals and again activated expression of $Kras^{G12D}$ with AdCre transduction. We again observed increased Fe^{2+} levels at 72 h after AdCre (Fig. 2, A and D; and Fig. S1 D). Similarly, we observed increased intracellular ferrous iron in both HPDE (immortalized human pancreatic ductal epithelial cells) and HBEC cells (immortalized human bronchial epithelial cells) after the expression of *KRAS*^{G12D} by lentiviral transduction (Fig. 2 E). Evaluation of a larger panel of human malignant cell lines from PDA and breast cancer confirmed that cells harboring mutant *KRAS* had consistently higher levels of total intracellular ferrous iron (Fig. S1 E). We next deployed previously reported genetically engineered mouse PDA cancer cell lines (designated *iKras*^{G12D}) in which the expression of *Kras*^{G12D} is dependent upon continuous doxycycline exposure (Ying et al., 2012) to probe the requirement for sustained oncogenic *KRAS* signaling to support iron metabolism and transport. We observed decreased intracellular labile Fe^{2+} within 48 h of doxycycline withdrawal in two *iKras* lines: AK196 and AK210 (Figs. 2 F and S1 F). These results demonstrate early and sustained increases in Fe^{2+} as a consistent effect of oncogenic *KRAS* expression and distinctly uncouple Fe^{2+} accumulation from cellular proliferation in primary cells, since replicative arrest (i.e., oncogene-induced senescence) is observed in the Fe^{2+}-rich state upon acute induction of *KRAS*^{G12D} signaling.

We next examined the transcription of a panel of iron regulatory genes in three nontransformed cell lines: HPDE, AALE (immortalized alveolar airway epithelial cells), and MEFs, with or without the expression of oncogenic *KRAS*. We observed significant elevation of *STEAP3* expression and decreased *FPN* (ferroportin, an iron exporter) expression in the presence of oncogenic *KRAS* (Fig. 2 G; and Fig. S1, G and H). Conversely, abrogation of oncogenic KRAS expression after Dox withdrawal in *iKRAS* cell lines (AK196, AK210, and AK38) resulted in directionally opposite effects on *STEAP3* and *FPN* (Figs. 2 H and S1 I). These data suggest that oncogenic *KRAS* is necessary and sufficient to maintain an elevated ferrous iron pool, at least in part by increased expression of ferrireductase and reduced iron efflux at a transcription level. Finally, overexpression of *STEAP3* in *iKRAS* cell lines (AK196 and AK210) led to a moderate elevation of Fe^{2+} in the absence of oncogenic KRAS but exhibited no additional additive effect on Fe^{2+} levels when oncogenic KRAS is present (Figs. 2 I and S1 J). This suggests that oncogenic *KRAS* establishes an elevated basal level of labile Fe^{2+} in the cancer cell, but that homeostatic control over this new state is retained, and thus cannot be further augmented by, for example, overexpression of *STEAP3*.

FeADC targets KRAS-induced cell state

KRAS is the most commonly mutated oncogene in human cancer but has proven difficult to target pharmacologically. RAF-MEK-

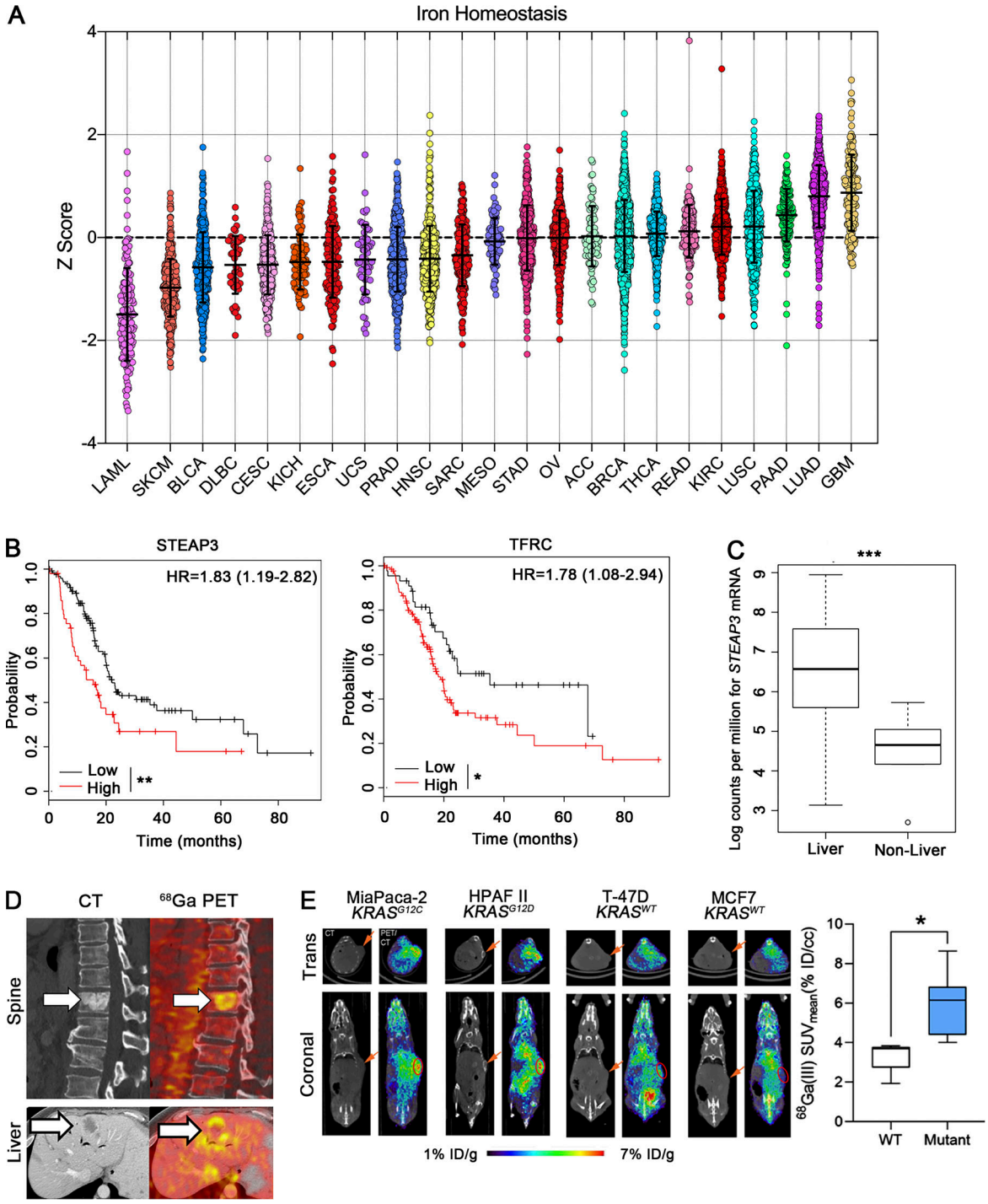

Figure 1. **A ferrous iron signature is prognostic in pancreatic adenocarcinoma. (A)** Pan cancer analysis of iron homeostasis. Z-sores are plotted for each of 23 tumor types. Medians for each tumor type are ranked from lowest to highest (L→R). Error bars represent mean ± SEM. **(B)** PAAD patients were binarized into high (upper half) or low (lower half) of mRNA expression of *STEAP3* and *TFRC*. Survival in months was estimated by the method of Kaplan and Meir (log-rank test, **, P < 0.01; *, P < 0.05). HR = hazard ratio for overall survival. **(C)** Boxplot showing median *STEAP3* expression in hepatic metastases vs. other metastatic sites in PDA patients profiled in Aguirre et al. (2018). ***, P < 0.001. **(D)** Representative CT (left) and fused Ga^{68} citrate PET/CT (right) images demonstrating Ga^{68} citrate avid metastases within the T10 vertebral body and liver from two patients with PDA. White arrows indicate metastatic sites. **(E)** Representative Ga^{68} PET images of mice bearing xenografts with wild-type or mutant *KRAS*. Tumors bearing an oncogenic *KRAS* mutation have an increased avidity for Ga^{68}. Error bars represent mean ± SEM, *n* = 3 mice/group and analyzed by a two-sample *t*-test. *, P < 0.05. Orange arrows (E) indicate the site of subcutaneous flank tumors in mice on CT.

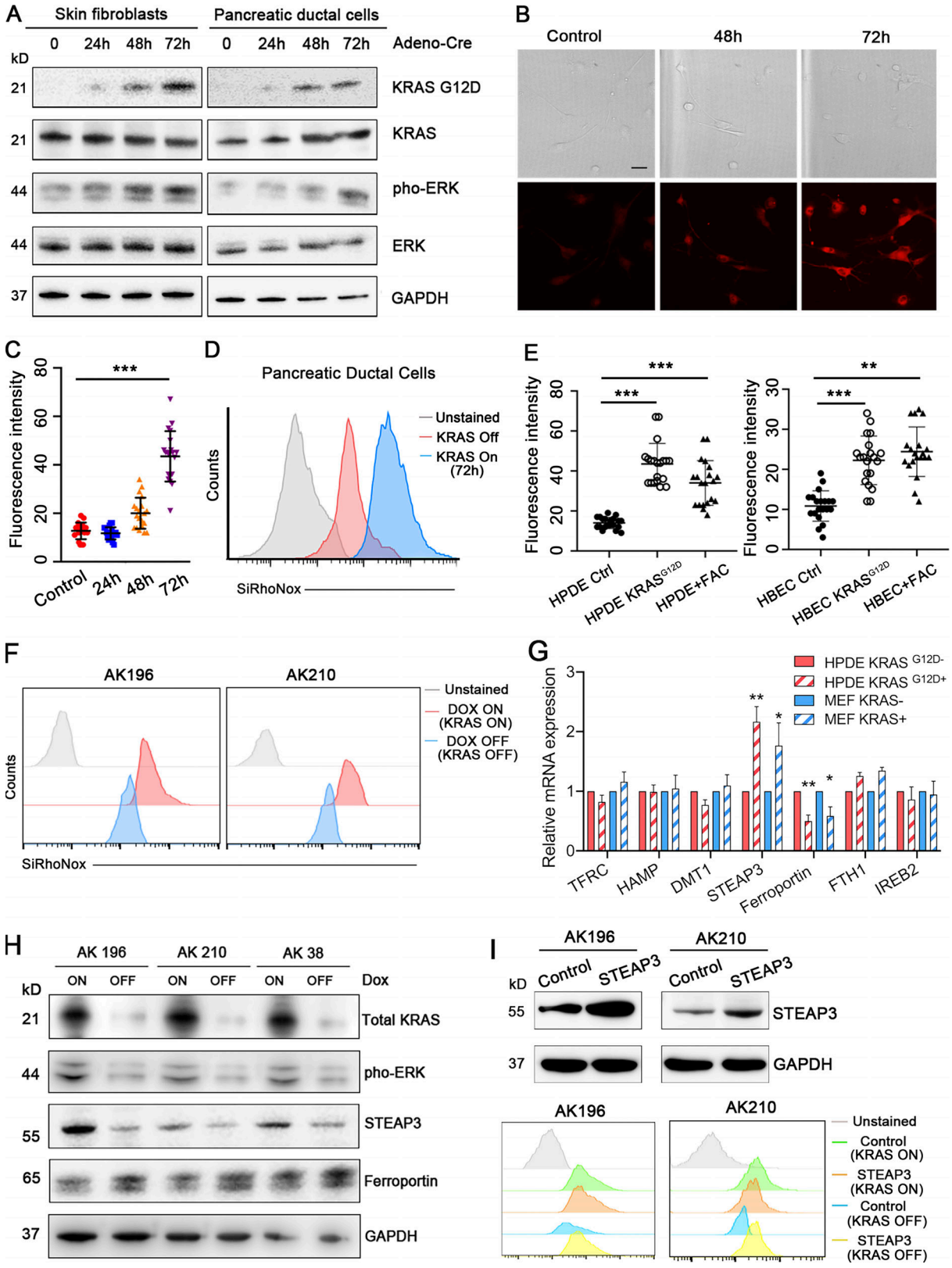

Figure 2. **Oncogenic *KRAS* drives an accumulation of labile ferrous iron. (A)** Western blot for KRAS^{G12D}, KRAS, phosphorylated ERK, and total ERK in *LSL-Kras^{G12D}*, *p53$^{f/f}$* mouse pancreatic ductal cells, and *LSL-Kras^{G12D}* mouse fibroblasts before and after treatment with AdCre at 24, 48, and 72 h. **(B and C)** Representative images of bright field and IF staining for SiRhoNox in *LSL-Kras^{G12D}* mouse fibroblasts. Quantifications of the fluorescence intensity per cell are plotted in C. Scale bar: 10 µm. **(D)** Representative histogram assessing staining for SiRhoNox by flow cytometry in *LSL-Kras^{G12D}*, *p53$^{f/f}$* mouse pancreatic ductal cells before and after the treatment with AdCre at 72 h. **(E)** Quantifications of the fluorescence intensity stained with SiRhoNox in HPDE, HPDE *KRAS^{G12D}* cells, and HPDE cells treated with ferric ammonium citrate (FAC). Also shown are the quantifications of the fluorescence intensity stained with SiRhoNox in HBEC,

HBEC *KRAS*^{G12D} cells, and HBEC cells treated with ferric ammonium citrate (FAC). **(F)** Representative histogram assessing staining with SiRhoNox by flow cytometry in *iKras* cells (AK196 and AK210) treated with or without doxycycline. **(G)** Quantitative PCR analysis of *TFRC*, *HAMP*, *DMT1*, *Steap3*, *ferroportin*, *FTH1*, and *IREB2* in HPDE, HPDE *KRAS*^{G12D} and MEF, MEF *KRAS* cells. **(H)** Western blot for total Kras, phosphorylated Erk1/2, STEAP3, and ferroportin in *iKras* cells treated with or without doxycycline. **(I)** Western blot for STEAP3 confirming the overexpression of STEAP3 in *iKRAS* cells (upper row). Representative histogram assessing staining with SiRhoNox by flow cytometry in control or STEAP3-overexpressed *iKras* cells treated with or without doxycycline (lower row). Each panel in D–F and I is representative of at least two independent experiments. Error bars represent mean ± SEM, n = 10 cells/group in B, n = 20 cells/group in C and E analyzed by a two-sample t-test. Significance in G was determined by one-way ANOVA and shown as *, $P < 0.05$; **, $P < 0.01$; and ***, $P < 0.001$.

MAPK is the major RAS effector arm in PDA (Collisson et al., 2012), acute myeloid leukemia (Burgess et al., 2017), and lung adenocarcinoma (Karreth et al., 2011). Fe^{2+}-dependent pharmacology (wherein a drug is activated through Fenton-type reaction with ferrous iron) has been established in the antimalarial artemisinin and related compounds but is mostly unexplored outside of antiprotozoal therapies. Since we found elevated Fe^{2+} levels to be driven by oncogenic *KRAS*, we hypothesized that mutant *KRAS*-driven PDA tumor cells might be selectively targeted with a FeADC based on 1,2,4-trioxolane ("TRX") chemistry (Fontaine et al., 2014). To determine whether a FeADC approach might be effective in mutant *KRAS*-driven malignancies, we studied PDA cells with the Fe^{2+} probe TRX-PURO, a Fe^{2+}-activatable conjugate of the aminonucleoside puromycin (Spangler et al., 2016b). Puromycin is released from TRX-PURO in cells selectively via reaction with Fe^{2+} (Fig. 3 A), and PURO release can be quantified with an anti-puromycin antibody. We treated primary skin fibroblasts harboring Cre-inducible *KRAS*^{G12D} with TRX-PURO after synchronously inducing high levels of oncogenic *KRAS*^{G12D}. We observed a time-dependent increase in puromycin signal out to 72 h after infection (Fig. S1 K), closely mirroring our findings with SiRhoNox (Fig. 2, B–D) and indicating efficient Fe^{2+}-dependent activation of TRX-PURO in cells expressing oncogenic *KRAS*.

Having established that mutant RAS signaling elevates intracellular Fe^{2+}, as measured with both SiRhoNox and TRX-PURO, we next sought to target the RAF-MEK-ERK pathway in PDA with a conditionally activated (FeADC-type) inhibitor of this pathway. Targeting MEK with allosteric inhibitors of MEK1/2 has shown clinical benefit, but the approach suffers from on-target toxicities that are dose-limiting in the eye, skin, gut, and other organs. Clinical experience has shown that sustainable dosing of these agents is typically only ∼25% of the FDA-approved dose (Saunders et al., 2020) severely hampering the dose intensity achievable in the tumor cell and ultimately limiting clinical efficacy. To model MEK inhibitor toxicity in animals, we administered the MEK inhibitor binimetinib to healthy mice for 3 wk. We observed thinning of the epidermal keratinocyte layer in tail skin (Fig. S2 A), confirming the conserved, essential role for MEK1/2 in the cellular epidermal layer (Azan et al., 2017; Danilenko et al., 2016). We hypothesized that a FeADC targeting MEK1/2 would be efficiently activated by Fe^{2+} in oncogenic *KRAS*-driven tumors, but not in healthily mouse epidermis, where normal iron homeostasis is preserved. We synthesized FeADCs bearing the FDA-approved allosteric MEK inhibitor cobimetinib (COBI) and based on either enantiomeric form of the Fe^{2+}-targeting TRX moiety, yielding the novel agents (*R*,*R*)-TRX-COBI and (*S*,*S*)-TRX-COBI (Fig. 3, A and B). Incubation of these FeADCs in mouse and human liver microsomes revealed somewhat superior metabolic stability of (*R*,*R*)-TRX-COBI (Table S1), and so, we used this form in subsequent studies (henceforth denoted simply TRX-COBI). We next evaluated the pharmacokinetic properties of TRX-COBI in NSG (NOD scid gamma) mice following a single 15 mg/kg dose by the intraperitoneal (IP) route. We observed a favorable exposure profile, with an elimination half-life of ∼6.9 h, C_{max} = 1,421 ng/ml, and AUC_{inf} = 6,462 h ng/ml (full parameters provided in Table S2). Significantly, the extent of free COBI released from its FeADC form was minimal, ∼2% of the total dose by C_{max} and AUC_{inf}. Overall, the pharmacokinetic properties of TRX-COBI were similar to that reported previously for COBI in Nu/Nu mice (Choo et al., 2012), suggesting TRX-COBI as a suitable comparator and FeADC prototype for in vivo study.

We compared the growth inhibitory effects of TRX-COBI and COBI across a panel of human PDA cells harboring oncogenic *KRAS* and found that TRX-COBI was efficiently activated, as evidenced by similar phospho-ERK reductions at equimolar exposure of COBI (Fig. 3 C). We further explored the relationship(s) among cell type, cell genotype, and TRX-COBI activation in an unbiased manner using the PRISM platform (Yu et al., 2016). We screened COBI and TRX-COBI in eight-point dose response across 750 cancer cell lines spanning 18 tumor types. Briefly, cell lines were treated with inhibitors for 5 d, and proliferation measurements allowed growth inhibitory doses (GI50) of TRX-COBI and COBI for each cell line to be calculated as described (Yu et al., 2016). We next calculated a TRX-COBI susceptibility ratio (i.e., $GI50_{COBI}/GI50_{TRX\text{-}COBI}$) for 520 out of 750 cell lines passing the criteria needed for index creation. PDA-derived cell lines exhibited the highest mean TRX-COBI GI50 ratio across the 18 types of tumor cells interrogated (Fig. 3 D). Additionally, *BRAF*- and *RAS*-mutated cancer cell lines also had significantly higher TRX-COBI GI50 ratios than wild-type *RAS* lines ($P < 0.001$; Fig. 3 E), indicating more efficient activation of the FeADC in MAPK-driven tumor cells and in PDA in general.

To show that TRX-COBI activation is Fe^{2+} dependent in PDA cells, we used shRNA to deplete *STEAP3* in MiaPaca2 and Capan1 cells and observed the expected decrease (∼50%) in intracellular Fe^{2+} levels as measured by SiRhoNox (Fig. S2 C). Importantly, STEAP3 depletion also decreased the conversion efficiency of TRX-COBI to COBI as measured by phospho-ERK/ERK ratios (Fig. S2, D and E). Since FeADC activation involves Fenton chemistry and the formation of ROS as reaction intermediates (Spangler et al., 2016a), we considered whether ferroptosis (Dixon et al., 2012) induction might contribute to cell killing by TRX-COBI treatment. Contrary to this hypothesis, we observed similar levels of lipid peroxidation and ROS generation in untreated, COBI, and TRX-COBI–treated MiaPaca2 cells (Fig. S2, F and G). Furthermore, we found in both MiaPaca2 and

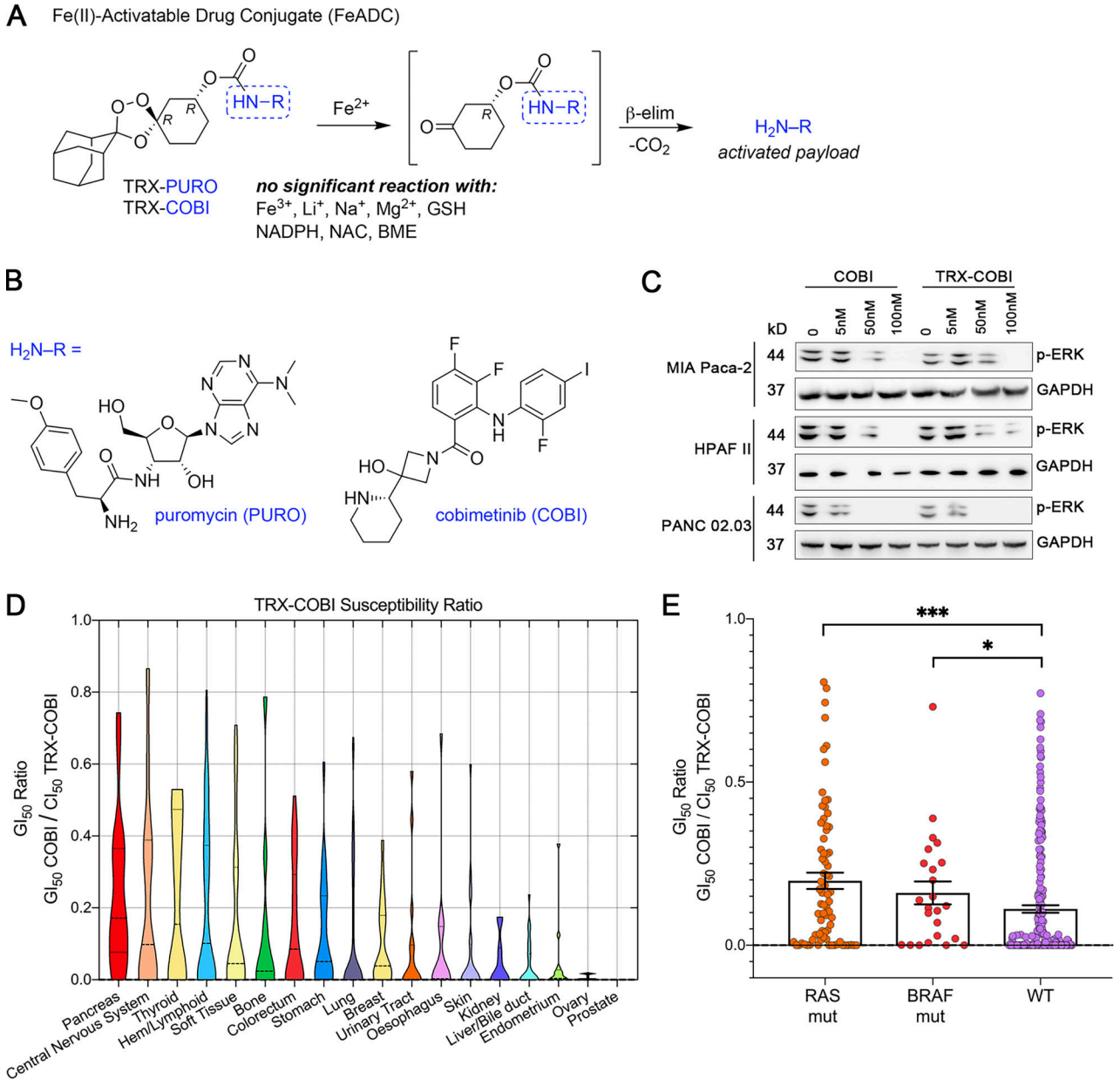

Figure 3. **FeADC targets elevated ferrous iron in PDA. (A)** Structure and mechanism of FeADC activation by ferrous iron sources. **(B)** Chemical structure of FeADC payloads puromycin (PURO) and cobimetinib (COBI). The tyrosyl amine and piperidine nitrogen atom are respectively the sites of conjugation in FeADC forms. **(C)** Western blot for phosphorylated ERK in COBI or TRX-COBI treated MIAPaca-2, HPAFII, and PANC 02.03 cells at indicated doses. **(D)** A large panel of cancer cells was treated with COBI and TRX-COBI for 5 d in PRISM screen. The GI50 of TRX-COBI for each cell was normalized by that of the GI50 to parent COBI to generate a TRX susceptibility ratio for each cell line. **(E)** *RAS*, *BRAF* mutation status, and GI_{50} ratios from PRISM screen. Error bars represented mean ± SEM in E. Significance in E was determined by a two-sample *t*-test and shown as *, P < 0.05 and ***, P < 0.001.

PANC02.03 cells that the cell death induced by COBI or TRX-COBI was not rescued by the antioxidant ferrostatin-1 nor by the iron chelator desferrioxamine (DFO), whereas cell death was induced by the bona fide ferroptosis inducer erastin (Fig. S2 H). These findings indicate that TRX-COBI induces nonferroptotic cell death through payload (COBI) release and MEK inhibition.

Together, the cellular data indicated that a prototypical MEK inhibitor FeADC is effective in *KRAS*-driven PDA cells and that FeADC activation depends, at least in part, on the cellular ferroreductive machinery under partial control of oncogenic *KRAS*.

An FeADC of COBI exhibits potent antitumor activity in vivo

We next evaluated the FeADC approach to MEK1/2 inhibition in vivo. We orthotopically implanted mouse $Kras^{LSL\_G12D}$, $Trp53^{f/+}$, $Pdx1^{Cre}$ (KPC) cells into syngeneic FVB mice and treated with equimolar doses of either TRX-COBI or COBI. Both drug forms were comparably growth inhibitory (Fig. 4, A and B) and showed equivalent suppression of phospho-ERK levels, at equimolar doses in this orthotopic PDA model (Fig. 4, G and H). We next evaluated the effects of COBI and TRX-COBI on overall survival in a widely used autochthonous $Kras^{LSL\text{-}G12D/+}$;

Trp53$^{flox/flox}$, (*KP*) mouse lung cancer model (Jackson et al., 2001). We initiated treatment with equimolar doses of COBI, TRX-COBI, or vehicle 8 wk after adenoviral tumor induction for 60 d. Mice receiving either COBI or TRX-COBI had fewer lung lesions (as evidenced by LSL-Tomato fluorescence) and showed prolonged overall survival compared to vehicle-treated mice (Fig. 4, C and D). We further examined the therapeutic efficacy of TRX-COBI in patient-derived xenograft (PDX) models. We used two *KRAS*^{G12D}-driven PDA PDX models (PDX260) and a *KRAS*^{G12C}-driven nonsmall cell lung cancer (NSCLC) PDX (PDX TM00186). Equimolar dosing of COBI or TRX-COBI significantly inhibited tumor growth relative to vehicle-treated tumors (Fig. 4, E and F). In addition, tumor lysates and tumor immunohistochemistry from PDA260 showed that TRX-COBI reduced phospho-ERK as effectively as parental COBI (Fig. 4, G and H). Collectively, these data demonstrate equivalent in vivo antitumor activity with equimolar doses of TRX-COBI or COBI in multiple relevant oncogenic *KRAS*-driven models of lung and pancreatic adenocarcinoma in vivo.

FeADC approach mitigates MEK inhibitor on-target, off-tumor toxicities

We next asked whether the FeADC approach might mitigate on-target, off-tumor toxicities of systemic MEK inhibition, reasoning that TRX-COBI should remain inactive (TRX-caged) in normal tissues (skin, retina) that are adversely impacted by systemic MEK inhibition in cancer patients. We used retinal cells and keratinocytes as experimentally tractable models of two tissues of known MEK inhibitor toxicity. We found that human retinal pigment epithelial cells (RPE-1) and keratinocytes (HaCaT) were about 10-fold less sensitive than PDA cells to TRX-COBI, as evidenced by intact phospho-ERK levels in the nontumor cells at drug concentrations sufficient to completely abolish phospho-ERK in PDA cells. In stark contrast, COBI more potently inhibited phospho-ERK in keratinocytes than in PDA cells (Fig. 5 A). Furthermore, uninduced *iKras* cells were resistant to TRX-COBI inhibition of MEK but were sensitive to COBI inhibition of MEK as measured by phospho-ERK levels (Fig. 5 B). These results suggest that the FeADC approach can realize improved therapeutic index in *KRAS*-driven cancers.

Next, we explored the tissue-selective activation of FeADCs in animals. We administered a single, equimolar dose of TRX-COBI, COBI, or vehicle, to mice bearing subcutaneous SW1990 and MiaPaca2 tumors in each flank followed 7 h later by collection of tissue from brain, liver, spleen, tail skin, plasma, and tumor. We calculated a COBI exposure ratio by dividing the concentration of free COBI in the tumor/tissues of mice receiving TRX-COBI with those receiving COBI directly, that is, COBI exposure ratio = $[COBI]_{TRX\text{-}COBI\ treated}/[COBI]_{COBI\ treated}$. We observed higher COBI exposure ratios in both SW1990 and MiaPaca2 tumors compared to plasma, liver, and spleen (Fig. 5 C). Phospho-ERK was significantly and comparably reduced in tumor and nontumor tissues of the COBI-treated mice, reflecting unsurprisingly equivalent MEK inhibition in tumor and healthy tissues alike. In contrast, phospho-ERK was extinguished in the tumors of TRX-COBI-treated mice to an equivalent degree as in COBI-treated mice, while phospho-ERK was spared (similar to vehicle control) in the brain, spleen, liver, and tail skin (Figs. 5 D and S3 A). This effect was consistent with the higher COBI exposure ratios observed in tumor vs. normal tissues and indicates that TRX-COBI remains mostly caged and thus inactive in normal tissues of tumor-bearing animals while still extinguishing KRAS-induced MAPK signaling in the tumor itself via KRAS-driven uncaging of COBI payload. To model the cumulative toxicities of chronic, systemic MEK inhibition, we collected tail skin samples from mice dosed with equimolar amounts of TRX-COBI, COBI, or vehicle for 20 d and measured the cellular epidermal layer. We consistently observed thinning of the epidermal layer in mice dosed with COBI (Figs. 5 E and S3 B) but not in TRX-COBI–dosed animals. Together, these findings show that many of the MEK1/2-dependent (on-target) extratumoral toxicities (Scholl et al., 2009; Balagula et al., 2011) of MEK inhibition are substantially mitigated by the FeADC approach, which might improve the poor therapeutic index of RAS-RAF-MAPK blockade in the clinic.

MEK inhibition with FeADC form enables dose intensity in combination therapies

The inherently low therapeutic index of MEK inhibitors has hindered development of MEKi-containing therapeutic combinations. Our encouraging data with TRX-COBI monotherapy suggested that MEKi-anchored combination treatment schemes might be better tolerated with an FeADC, due to relatively less active MEK inhibition in off-target tissues. Inhibition of SHP2 can sensitize many cycling-dependent *KRAS*-mutant or *KRAS*-amplified cancers to MEK inhibitors (Ruess et al., 2018). While such vertical blockade holds tremendous promise, combination therapy of SHP2 and MEK inhibitors negatively effects tolerability in mice (Fedele et al., 2018). Indeed, we found that combinations of tolerable monotherapy doses of COBI and the SHP2 inhibitor SHP099 (Novartis) induced study-terminating body weight loss from baseline within 3 wk when combined in non–tumor-bearing NSG mice (Fig. S4 A).

We next compared the efficacy and tolerability of TRX-COBI to COBI when anchoring combination therapy with the SHP2 inhibitor RMC-4550 (Revolution Medicines) in *KRAS*^{G12C} NSCLC (TM00186) PDX model. Six separate groups of mice were administered vehicle, 30 mg/kg RMC-4550 monotherapy, or combinations comprising 30 mg/kg of RMC-4550 combined with COBI at either 7.5 mg/kg or 10 mg/kg, or RMC-4550 with comparable (equimolar) 12.5 mg/kg or 16 mg/kg doses of TRX-COBI. Of note, mice receiving the combination of COBI 10 mg/kg plus RMC 30 mg/kg lost weight (~10%; Fig. 6 A) and exhibited lassitude. Tumor and spleen lysates both showed profound inhibition of the generation of phospho-ERK (Fig. 6, C and D). Remarkably, the equivalent combination of TRX-COBI 16 mg/kg with RMC 30 mg/kg induced more pronounced tumor growth inhibition without measurable weight loss (Fig. 6 B) and showed comparatively minor effects on the levels of phospho-ERK in the spleen (Fig. 6, C and D).

To assess the potential of an FeADC to improve the toxicity profile of vertical MAPK pathway blockade, we next assessed cytotoxicity of combined MEK + SHP2 dual inhibition in PDA (MiaPaca2) vs. normal (RPE-1 and HaCaT) cells. Treatment of

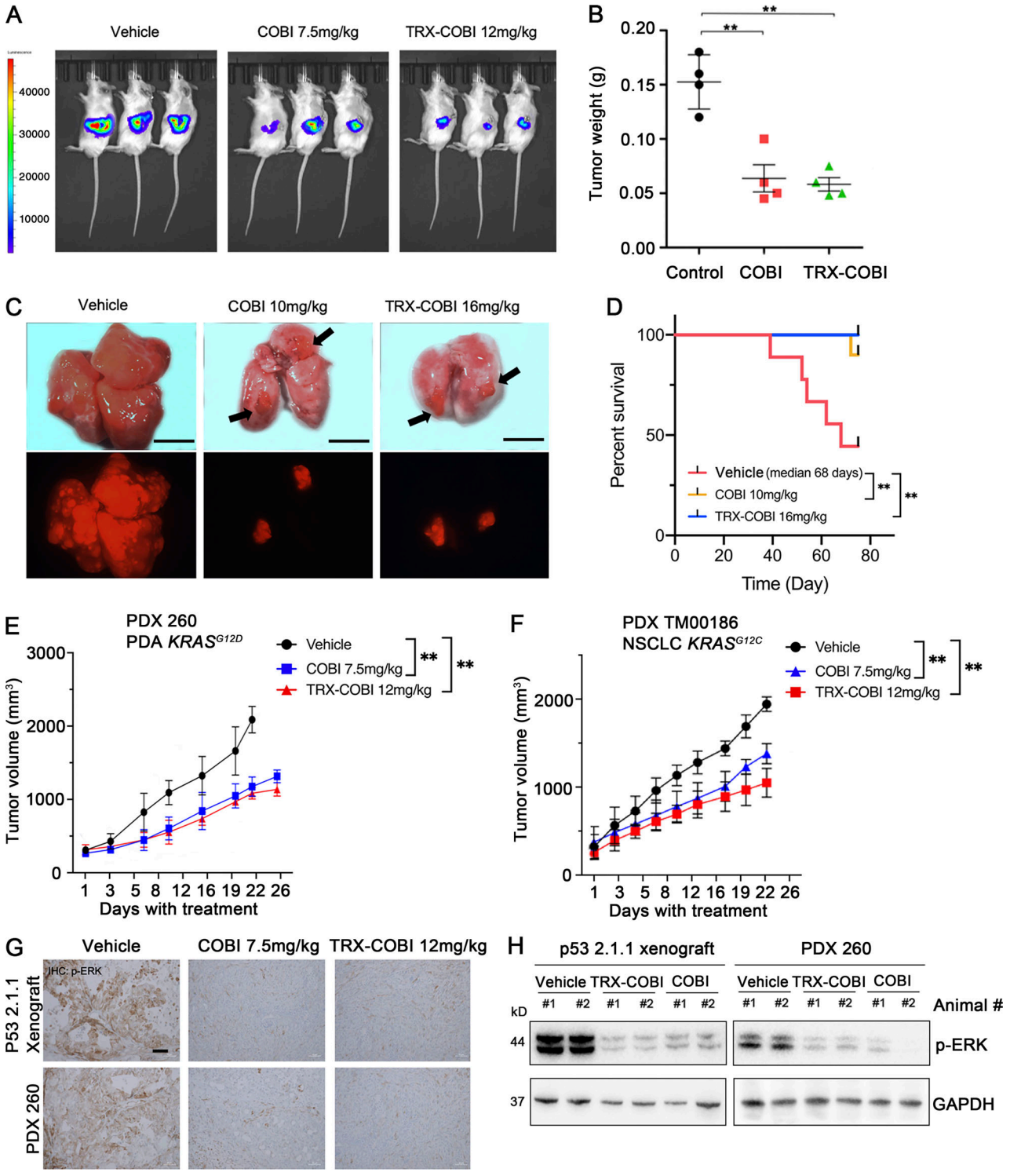

Figure 4. **An FeADC of COBI exhibits potent antitumor activity in vivo. (A)** Representative bioluminescence images of p53 2.1.1-fLuc orthotopic pancreas tumor xenografts treated with vehicle or the indicated, equimolar doses of COBI or TRX-COBI. **(B)** Tumor weights at the end point from A. Error bars represent mean ± SEM, *n* = 4–5 mice/group and analyzed by a two-sample *t*-test. **, P < 0.01. **(C)** Representative gross lung images in *KP* mouse model. Vehicle, equimolar doses of COBI, and TRX-COBI treatment started 8 wk after the adenoviral induction and continued for 60 d. Scale bar: 0.5 cm. **(D)** Overall survival of (C) analyzed by a log-rank test, *n* = 8–10 mice/group; **, P < 0.01. **(E and F)** Tumor volume changes (mean ± SEM; error bars) of mutant *KRAS* PDA and NSCLC PDX model, *n* = 8–10 mice/group. Data were analyzed by one-way ANOVA; **, P < 0.01. **(G)** IHC of xenografts from A and E (10×) stained with phosphorylated ERK. Scale bar: 50 µm. **(H)** Western blot for phosphorylated ERK of tumors resected at the end of treatment in A and E.

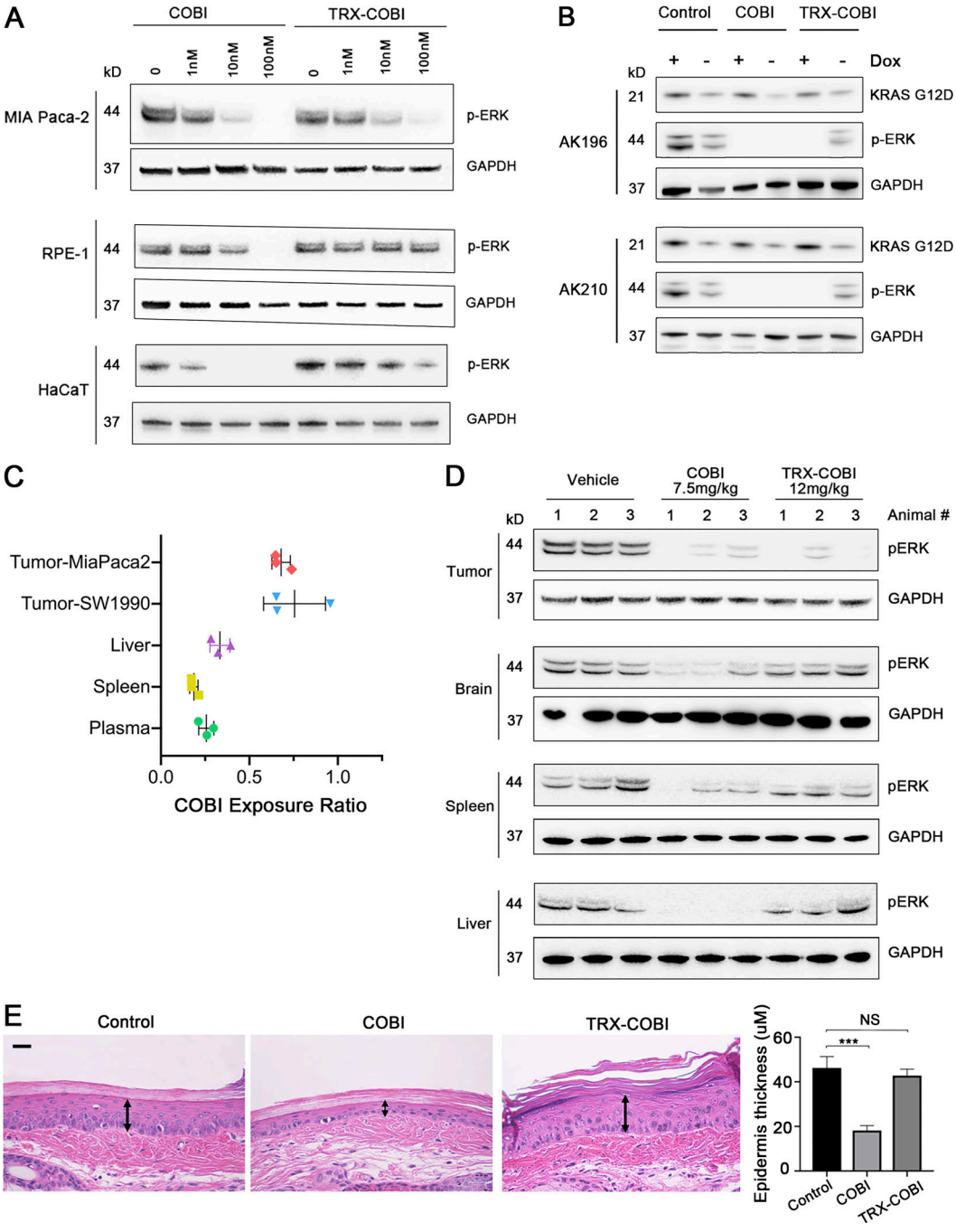

Figure 5. **FeADC approach mitigates MEK inhibitor off-tumor/on-target toxicities. (A)** Western blot for phosphorylated ERK of MiaPaca-2, RPE-1, and HaCaT cells treated with COBI and TRX-COBI at the indicated dose. **(B)** Western blot for $Kras^{G12D}$ and phosphorylated Erk1/2 in *iKras* cells with or without doxycycline for 48 h followed by treatment with COBI or TRX-COBI at 100 nM for 6 h. **(C)** COBI exposure ratios in tumors, plasma, spleen, and liver after treatment for 7 h. Data were determined by LCMS/MS assay. Error bars represent mean ± SEM. **(D)** Western blot for phosphorylated ERK of tumor xenografts, brain, spleen, and liver from NSG mice after treatment with the vehicle, the equimolar dose of COBI, and TRX-COBI for 8 h. **(E)** Representative images (40×) of H&E-stained mouse tail skin after the treatment with either vehicle or equimolar doses of COBI or TRX-COBI, for 20 d. Scale bar: 20 µm. Error bars represent mean ± SEM, n = 3 mice/group and analyzed by a two-sample t-test. ***, $P < 0.001$.

nonmalignant RPE-1 and HaCaT cells with increasing concentrations of COBI enhanced cell growth inhibition of SHP2 inhibitor (SHP099, 10 µM), while equimolar combinations of TRX-COBI/SHP2i were less toxic to these normal cells (Fig. S4, B and C). In contrast, $KRAS^{G12C}$ MiaPaca-2 cells showed equivalent sensitivity to the two combinations (Fig. S4 D), indicating a potentially improved safety profile with and comparable efficacy of TRX-COBI in MEK inhibitor–based combination therapies. Together, these data indicate that FeADC-based MEK inhibition combined with SHP2 blockade exhibits superior tolerability and improved efficacy in *KRAS*-driven tumors. Consistent with this interpretation, we observed that combining

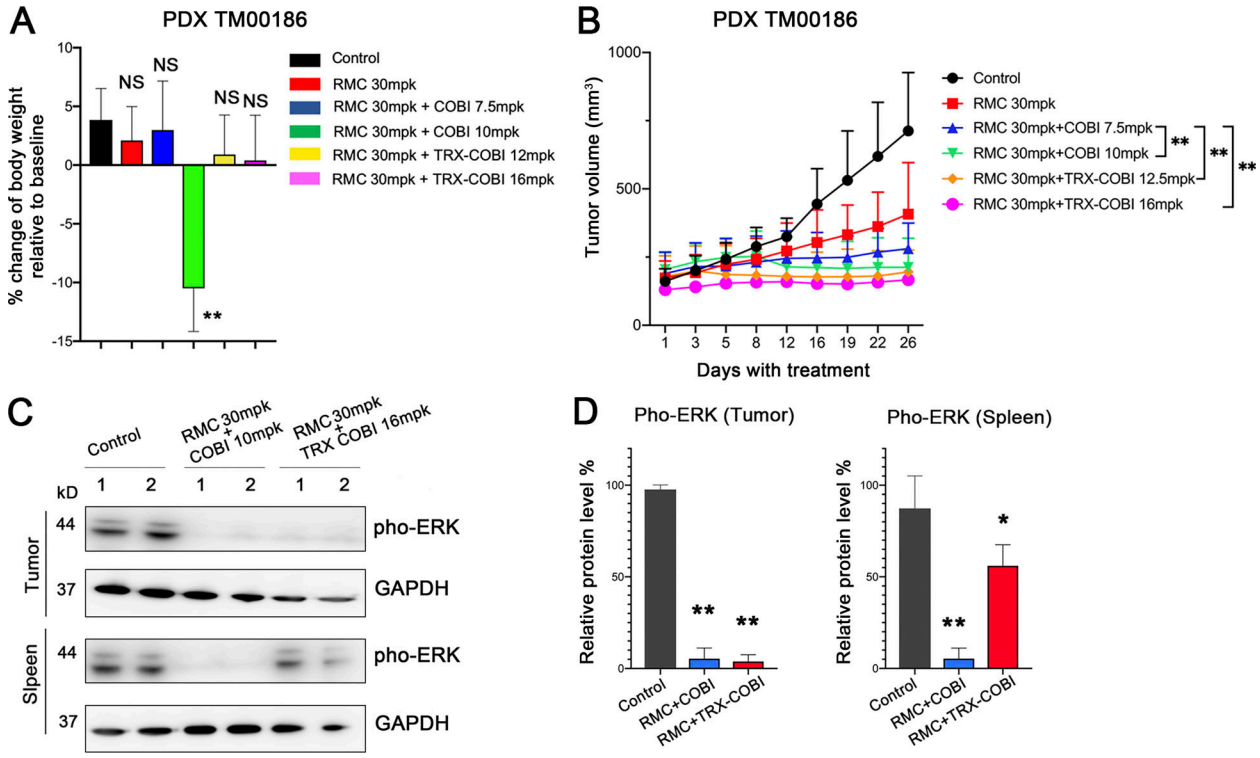

Figure 6. **MEK inhibition with FeADC enables dose intensity in combination therapies. (A)** Mouse body weight changes normalized to the baseline after the treatment with the vehicle, 30 mg/kg RMC-4550 monotherapy, or combinations comprising 30 mg/kg RMC-4550 combined with COBI at either 7.5 mg/kg or 10 mg/kg or RMC-4550 with comparable (equimolar) 12.5 mg/kg or 16 mg/kg doses of TRX-COBI. Error bars represent mean ± SEM, *n* = 6 mice/group and analyzed by a two-sample *t*-test. **, P < 0.01. **(B)** Tumor volume changes of PDX TM00186 tumors after the treatments in D. Error bars represent mean ± SEM, *n* = 6 mice/group and analyzed by one-way ANOVA; **, P < 0.01. **(C)** Western blot for phosphorylated ERK of tumor xenografts and spleen from NSG mice after treatment with vehicle, RMC 30 mg per kg (mpk) + COBI 10 mpk or RMC 30 mpk + TRX-COBI 16 mpk in the cohort of A and B. **(D)** Quantification of phosphorylated ERK expression in C, error bars represent mean ± SEM, and analyzed by a two-sample *t*-test. *, P < 0.1; **, P < 0.01.

TRX-COBI with a structurally distinct SHP2 inhibitor (SHP099) similarly improved tolerability (as judged by body weight) when compared to combinations involving COBI (Fig. S4 A).

Discussion

Iron homeostasis is tightly controlled at the level of the cell and organism (Torti and Torti, 2013b). Consistent with previous observations in breast cancer (Miller et al., 2011; Pinnix et al., 2010), prostate cancer (Tesfay et al., 2015), and glioblastoma (Schonberg et al., 2015), we have now confirmed an altered iron metabolic state in PDA characterized by the elevation of cytosolic labile ferrous iron. The metabolic or other benefits gleaned by the PDA cell through this change are unclear, but the liabilities it presents are obvious. Labile iron promotes Fenton chemistry and contributes to lipid peroxidation, thus making cells highly dependent on constitutive antioxidant responses mediated by GPX4 (Forcina and Dixon, 2019; Liu et al., 2018) and/or FSP1 (Bersuker et al., 2019; Doll et al., 2019) to avoid a default ferroptotic cell death program. On the one hand, our findings in oncogenic *KRAS*-driven cells and tumor models provide further evidence linking oncogenic *KRAS* to elevated Fe^{2+} and a vulnerability to ferroptosis (Dixon et al., 2012). Beyond this, we show that KRAS-driven "ferroaddiction" can be exploited with FeADC-based therapy independent of ferroptotic pathways.

The mechanism(s) by which specific oncogenes alter iron homeostasis to promote tumor growth remain to be fully elucidated. Here, we show that *KRAS* signaling is necessary and sufficient to empower Fe^{2+} demand in PDA cells. In particular, oncogenic *KRAS* exerts control over the sole iron exporter and lysosomal ferrireductase to maintain an expanded pool of bioavailable Fe^{2+}. *Ras* oncogenes have been shown to alter nutrient metabolism (Hensley et al., 2016; Perera and Bardeesy, 2015; Ying et al., 2012), so it is unsurprising that this control would extend to iron nutrient. Previously, oncogenic *H-Ras* was shown to repress Ferritin expression and thereby expand the labile iron pool and support tumor cell growth (Kakhlon et al., 2002). Notably, we find that oncogenic *KRAS* signaling does not appear to act on the ferritin axis, but significantly through *STEAP3* and *FPN*. Taken together, these findings suggest that oncogenes can employ diverse means to elevate labile iron, and that therapeutic modalities targeting labile iron directly (rather than indirectly via iron modulatory genes) may be effective across a broader range of cancers. Moreover, it has been widely demonstrated that multiple tumor local immune components, including tumor-associated macrophages and neutrophils, display a strong iron-release phenotype that promotes tumor cell proliferation and growth (Corna et al., 2010; Recalcati et al., 2010). Thus, we expect that the tumor-associated macrophages likely contribute to an iron-enriched tumor microenvironment which support the

observed increased intracellular iron storage in the mutant KRAS-driven tumor cells.

Most *KRAS*-mutant cancers depend on sustained expression and signaling of *KRAS*, thus making it a high-priority therapeutic target (Papke and Der, 2017; Stephen et al., 2014). Unfortunately, the development of direct small molecule inhibitors of mutant K/N/HRAS proteins has been elusive until very recently (Kim et al., 2020; Seton-Rogers, 2020). Moreover, single-agent inhibition of KRAS effectors (e.g., MEK-MAPK pathway) in *KRAS*-mutant cancers has been disappointing to date (Adjei et al., 2008; Infante et al., 2012; Ko et al., 2016; Zhao and Adjei, 2014). On-target MEK inhibition in healthy tissues dramatically limits the tolerable dose and also the feasibility of MEK inhibitor–based combination therapy. The cellular pathways influenced by dominant acting oncogenes are often essential for homeostatic maintenance of healthy tissues in patients. As a result, potent inhibitors of pathways downstream of mutated oncogenes often have deleterious effects in healthy tissues. This manifests as clinical toxicity. Furthermore, since pathway flux is often greater in cancer cells than in normal cells, the amount of inhibitor required for therapeutic efficacy in the tumor often closely approaches or even exceeds the dose that is tolerable clinically, due to toxicities in healthy tissues.

The Fe^{2+}-mediated Fenton reaction underlies the pharmacology of artemisinins and related endoperoxide antimalarials (Ansari et al., 2013; O'Neill and Posner, 2004). Leveraging this clinically proven chemistry, we introduced (Fontaine et al., 2014; Mahajan et al., 2012) the concept of FeADCs. Having uncovered in the current study an elevation of Fe^{2+} stemming from oncogenic RAS/MAPK signaling, we synthesized and evaluated TRX-COBI, a novel FeADC designed to target the MAPK pathway in *KRAS*-driven PDA. Notably, we show with TRX-COBI tumor-selective activation that enables ablation of MAPK signaling in PDA tumor cells and xenografts, while sparing the pathway in normal cells and tissues, including in major organs of iron storage (liver) and targets of MEK inhibitor–induced toxicity (skin and central nervous system). We thus decouple MAPK signaling from elevated Fe^{2+} status in normal and tumor cells and present a therapeutic strategy that exploits these distinctions to enable more tolerable and efficacious combination therapy targeting the MAPK pathway in *KRAS*-driven PDA. The discovery of pharmacologically exploitable ferroaddiction in *RAS*-driven cancers holds promise to improve the treatment of deadly cancers through a practicable and generalizable approach to FeADC design, development, and clinical testing.

Materials and methods

Key resources

Key resources are listed in Table S3.

Experimental model and subject details

Cell lines

MiaPaca-2, HPAF II, HPAC, Panc 10.05, and Panc 02.03 are from American Type Culture Collection. Capan1 was provided by S.K. Batra (University of Nebraska, Lincoln, NE). MDAMB231, MDAMB468, ZR75-1, SKBR3, and T47-D were provided by M.M. Moasser (University of California, San Francisco [UCSF], San Francisco, CA). *iKras* lines AK38, AK196, and AK210 were provided by R. Perera (UCSF, San Francisco, CA). Skin fibroblast isolation from *LSL-KRAS^{G12D}* mouse was performed as described (Khan and Gasser, 2016). Cells were maintained at 37°C in a humidified incubator at 5% CO_2. Cells were grown in appropriate media as recommended by ATCC and supplemented with 10% FBS (Gibco) and 1% penicillin/streptomycin (Gibco). All cell lines tested were negative for mycoplasma contamination.

Patient characteristics and accrual

This study was approved by the UCSF Institutional Review Board (IRB) and was compliant with the Health Insurance Portability and Accountability Act. Informed consent was obtained from all patients enrolled into the study.

Patient inclusion criteria were (1) histologically confirmed/clinically suspected pancreatic cancer, (2) at least one lesion ≥1 cm, (3) age >18, (4) a signed informed consent indicating that they are aware of the investigational nature of this study, (5) negative for HIV, and (6) not be pregnant or breastfeeding.

Patient demographic information including age and sex were recorded as well as their tumor locations and histological grade.

Mice models

All experiments were conducted in the AAALAC-accredited UCSF in accordance with all applicable local requirements, including approval by the IACUC.

Small animal PET/computed tomography (CT) and biodistribution studies. 6-wk-old male NSG mice were purchased from Jackson Laboratory.

Orthotopic pancreas xenografts. Derivation of the p53 2.1.1 FVB/n mice has been described (Collisson et al., 2012).

KPT *lung tumor model.* *Kras$^{LSL\text{-}G12D/+}$,p53$^{flox/flox}$,R26$^{LSL\text{-}tdTomato}$* (*KPT*) mice have been previously described. Mice were bred on a mixed background.

PDXs. For generation of the PDX 260 model, informed consent was obtained from the patient as per an open IRB-approved protocol at UCSF. Tumors were implanted in NSG mice (Jackson Laboratory).

Method details

Reagents and antibodies

The following antibodies were used: KRAS G12D (14429; dilution: 1:1,000; Cell Signaling Technology); KRAS (53270; dilution: 1:1,000; Cell Signaling Technology); phospho-Erk1/2 (Thr202/Tyr204; 4370; dilution: 1:1,000; Cell Signaling Technology); Erk1/2 (4696; dilution: 1:1,000; Cell Signaling Technology); GAPDH (5,174; dilution: 1:1,000; Cell Signaling Technology); STEAP3 (17186; dilution: 1:1,000; Proteintech); and ferroportin (NBP1-21502SS; dilution: 1:1,000; Novus Biologicals). COBI and SHP099 were purchased from MedChemExpress. RMC-4550 material used in these studies was provided by Revolution Medicines, Inc., in collaboration with Sanofi, Paris, France.

General synthetic methods

All reactions were performed under an Argon atmosphere using anhydrous solvents obtained from commercial suppliers in

oven-dried, round-bottom flasks containing Teflon-coated stirrer bars, unless otherwise noted. All anhydrous solvents used were purchased from Sigma-Aldrich and used without further purification. Solvents used during flash column chromatography and reaction workup procedures were purchased from either Sigma-Aldrich or Fisher Scientific and were used without further purification. All other reagents were obtained commercially and used without further purification, unless otherwise stated. Air and/or moisture sensitive reagents were transferred via syringe and were introduced into reaction vessels through rubber septa. Reactions were monitored using TLC, performed on 0.25-mm EMD precoated glass-backed silica gel 60 F-254 plates. Column chromatography was performed on Silicycle Sili-prep cartridges using a Biotage Isolera Four automated flash chromatography system. Compounds were visualized under UV light or through staining with permanganate, iodine, or most preferably for trioxolane analogs, Seebach's "Magic" stain (composed of the following: 2.5 g phosphomolybdic acid, 1.0 g cerium sulfate, 6 ml concentrated sulfuric acid, and 94 ml water). Solutions containing crude reaction mixtures, as well as those obtained upon reaction workup, and chromatography fractions were first concentrated by rotary evaporation at temperatures under 40°C, at 20 Torr and then subsequently placed under Hi-Vac at 0.5 Torr, unless otherwise indicated. (R)- and (S)-4-nitrophenyl carbonate intermediates were prepared as reported previously (Blank et al., 2020).

Instrumentation

NMR spectra were recorded on a Bruker Avance III HD 400 MHz (with 5 mm BBFO Z-gradient Smart Probe), calibrated to CH(D)Cl3 as an internal reference (7.26 and 77.00 ppm for 1H and 13C NMR spectra, respectively). Data for 1H NMR spectra are reported in terms of chemical shift (δ, ppm), multiplicity, coupling constant (Hz), and integration. Data for 13C NMR spectra are reported in terms of chemical shift (δ, ppm), with multiplicity and coupling constants in the case of C–F coupling. The following abbreviations are used to denote the multiplicities: s = singlet; d = doublet; t = triplet; q = quartet; quin = quintet; sept = septet; m = multiplet; app = apparent; or combinations of these. Where required, COSY, HSQC, and HMBC were used for the assignment of protons and carbons. Liquid chromatography mass spectrometry (LCMS) and compound purity were determined using Waters Micromass ZQ 4000, equipped with a Waters 2795 separation module, a Waters 2996 photodiode array detector, and a Waters 2424 ELSD. HPLC was performed on a Waters 2535 separation module with a Waters 2998 photodiode array detector using an XBridge BEH C18, 3.5 µm, 4.6 × 20 mm column, at ambient temperature (unregulated) using a mobile phase of water–methanol containing a constant 0.05% formic acid. High-resolution mass spectroscopy (HRMS) spectra were obtained using a Finnigan LTQFT mass spectrometer by the mass spectrometry facility at the University of California, Berkeley. All compounds synthesized were ≥95% pure as determined by LCMS and 1H, 13C, and 19F NMR.

Synthetic procedures for (1″R, 3″R)-TRX-COBI and (1″S, 3″S)-TRX-COBI

To an oven-dried round-bottom flask containing a magnetic stir bar under an Ar(g) atmosphere was added COBI (0.150 mg, 0.28 mmol, 1.0 equivalents [equiv]) and (1″R,3″R)-dispiro[adamantane-2,3′-[1,2,4]trioxolane-5′,1″-cyclohexan]-3″-yl (4-nitrophenyl) carbonate (0.150 mg, 0.34 mmol, 1.2 equiv) followed by dimethylformamide (10 ml), N,N-diisopropylethylamine (0.30 ml, 1.74 mmol, 6.0 equiv), and 4-dimethylaminopyridine (0.038 g, 0.34 mmol, 1.2 equiv; Scheme 1). Reactions were stirred at room temperature (RT) for 3–72 h while monitoring reaction progress by LCMS. The reaction was then diluted with deionized H_2O (100 ml) and extracted with EtOAc (1 × 100 ml). The organic layer was washed repeatedly with a saturated aqueous (satd. aq.) $NaHCO_3$ solution until the aqueous layer was colorless and no longer yellow (indicating that most of the p-nitrophenol had been successfully removed from the organic layer). The organic layer was then dried (Na_2SO_4), filtered, and concentrated under reduced pressure to a viscous yellow oil. The crude material was then purified using flash column chromatography (40 g silica gel cartridge, initially using 0–50% EtOAc–Hexanes and then switching to 0–15% MeOH [containing 0.7 N NH_3]/CH_2Cl_2, product eluted during 40% EtOAc–Hex, unreacted COBI eluted during 15% MeOH [containing 0.7 N NH_3]/CH_2Cl_2 to yield the desired product [1″R,3″R] TRX-COBI [30–50%] as a colorless solid [9:1 diastereomeric ratio (dr), trans:cis]). 1H NMR (400 MHz, CDCl3) δ 8.60 (br s, 1H), 8.41 (br s, 1H), 7.39 (dd, *J* = 10.4, 1.6 Hz, 1H), 7.32 (d, *J* = 8.5 Hz, 1H), 7.15 (br s, 1H), 6.82 (app q, *J* = 8.3 Hz, 1H), 6.61 (app td, *J* = 8.5, 5.4 Hz, 1H), 5.45 (br s, 1H), 4.88 (br s, 1H, minor diastereomer), 4.76 (app sept, *J* = 4.5 Hz, 1H), 4.11–4.25 (m, 2H), 3.93–4.11 (m, 3H), 3.22–3.44 (m, 1H), 2.87 (br s, 1H), 2.07–2.25 (m, 1H), 1.86–2.02 (m, 8H), 1.72–1.85 (m, 7H), 1.46–1.65 (m, 6H), 1.21–1.46 (m, 3H); 13C NMR (100 MHz, CDCl3) δ 169.1, 155.4, 153.2 (br d, *J* = 249.7 Hz), 152.8 (br d, *J* = 253.4 Hz), 152.4 (br d, *J* = 251.2 Hz), 143.5 (br d, *J* = 246.1 Hz), 132.9 (d, *J* = 3.7 Hz), 132.6 (d, *J* = 3.7 Hz), 130.8 (d, *J* = 10.3 Hz), 124.4, 124.2, 119.9, 119.6, 119.2, 111.8, 111.8 (minor diastereomer), 109.1 (br d, *J* = 17.5 Hz), 108.5, 108.3, 81.6 (d, *J* = 7.3 Hz), 77.3, 72.0, 70.9 (br s), 65.2, 64.9, 60.3, 60.1, 48.0 (br s), 39.6, 36.7, 36.4, 36.3, 34.9, 34.7, 34.0, 33.9 (minor diastereomer), 30.5, 30.2 (minor diastereomer), 29.7, 26.9, 26.4, 25.4, 25.0 (br s), 24.1 (br s), 19.5, 19.4 (minor diastereomer), several minor diastereomer peaks overlapping or not observed; 19F NMR (376 MHz, CDCl3) δ −126.9, −127.0, −127.1 (br s), −131.3 (br s), −141.4 (br s); LRMS (ESI): *m/z* $[M + Na]^+$ calculated (calcd) for C38H43F3IN3O7Na: 860.20, found: 860.15, retention time = 13.1 min (diode array), HRMS (ESI) *m/z* $[M + Na]^+$ calcd for C38H43F3IN3O7Na: 860.1995, found: 860.1975.

To a 20-ml scintillation vial containing a magnetic stir bar under an Ar(g) atmosphere was added COBI (238 mg, 0.45 mmol, 2.50 equiv), (1″S, 3″S)-dispiro[adamantane-2,3′-[1,2,4]trioxolane-5′,1″-cyclohexan]-3″-yl (4-nitrophenyl)carbonate (80 mg, 0.18 mmol, 1.0 equiv), N,N-dimethylformamide (1.60 ml), N,N-diisopropylethylamine (78 µl, 0.45 mmol, 2.50 equiv), and 4-dimethylaminopyridine (28.6 mg, 0.23 mmol, 1.3 equiv; Scheme 2). The reaction was stirred at RT for 12 h and monitored by TLC and LCMS. The reaction was then diluted with satd. aq. $NaHCO_3$ (15 ml) and EtOAc (15 ml), and the layers were separated. The aqueous layer was further extracted with EtOAc (3 × 15 ml), and the combined organic phases were washed repeatedly with satd. aq. $NaHCO_3$ until the aqueous layer was colorless and no longer yellow (indicating that most of the p-nitrophenol

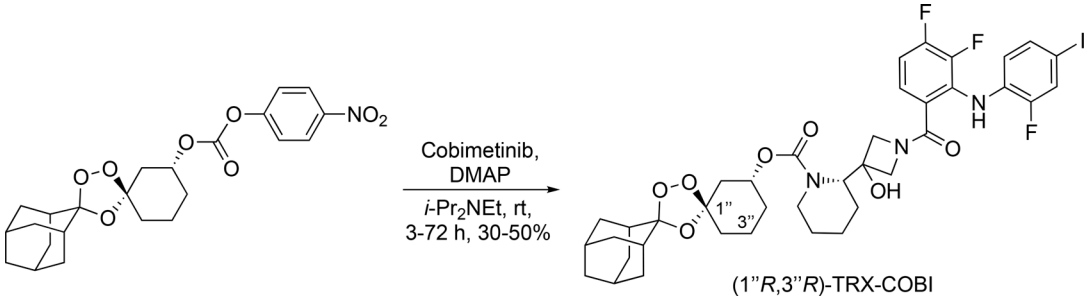

Scheme 1. (1"R, 3"R)-dispiro[adamantane-2,3'-[1,2,4] trioxolane-5',1"-cyclohexan]-3"-yl (S)-2-(1-(3,4-difluoro-2-((2-fluoro-4-iodophenyl)amino)benzoyl)-3-hydroxyazetidin-3-yl)piperidine-1-carboxylate.

had been successfully removed from the organic layer). The organic phase was then dried ($MgSO_4$), filtered, and concentrated under reduced pressure to afford a crude viscous yellow oil. The crude material was purified by preparative HPLC (40–100% MeOH–water + 0.05% formic acid), and the product-bearing fractions were combined, concentrated, and lyophilized to give (1"S,3"S)-TRX-COBI (65.2 mg, 0.078 mmol, 43%) as a colorless lyophilized solid (9:1 dr, trans:cis). 1H NMR (400 MHz, CDCl3) δ 8.57 (br s, 1H), 8.43 (br s, 1H), 7.41 (dd, *J* = 10.4, 1.8 Hz, 1H), 7.34 (br d, *J* = 8.8 Hz, 1H), 7.16–7.17 (m, 1H), 6.83 (br d, *J* = 7.1 Hz), 6.62 (td, *J* = 8.6, 5.4 Hz), 5.2–5.8 (m, 1H), 4.85–4.93 (m, 1H, minor diastereomer), 4.74 (br s, 1H), 4.09–4.29 (m, 2H), 3.91–4.09 (m, 3H), 3.40 (br s, 1H), 3.27 (br s, 1H), 2.92 (br s, 1H), 2.24 (br d, *J* = 12.2 Hz, 1H), 1.88–2.03 (m, 8H), 1.74–1.88 (m, 7H), 1.56–1.67 (m, 5H), 1.43–1.56 (m, 3H), 1.23–1.42 (m, 2H); 13C NMR (100 MHz, CDCl3) δ 169.1, 155.4, 153.7 (br d, *J* = 249.7), 152.7 (br d, *J* = 252.7), 152.6 (br d, *J* = 251.9), 143.5 (br d, *J* = 238.1 Hz), 132.9 (br d, *J* = 2.9 Hz), 132.4–132.7 (m), 132.1–132.4 (m), 130.8 (br d, *J* = 12.4 Hz), 124.4, 124.2, 119.8, 119.6, 119.3, 111.8, 111.8 (minor diastereomer), 109.2 (br d, *J* = 18.3 Hz), 108.6, 81.6 (d, *J* = 5.9 Hz), 77.2, 72.1, 72.0 (minor diastereomer), 70.9 (br s), 65.1, 64.9 (br s), 60.3, 60.1, 47.8 (br s), 40.0, 39.6 (minor diastereomer), 36.7, 36.3, 36.3, 34.8, 34.8, 33.9, 33.8 (minor diastereomer), 30.6, 30.2 (minor diastereomer), 26.9, 26.4, 25.4, 25.0, 24.1 (br s), 19.6, several minor diastereomer peaks overlapping or not observed; 19F NMR (376 MHz, CDCl3) δ −126.9, −127.1, −131.3 (dd, *J* = 7.5, 11.3 Hz), −141.4 (d, *J* = 19.1 Hz); LRMS (ESI): *m/z* [M + Na]$^+$ calcd for C38H43F3IN3O7Na: 860.20, found: 860.22, retention time = 13.58 min (ELSD); HRMS (ESI) *m/z* [M + Na]$^+$ calcd for C38H43F3IN3O7Na [M + Na]$^+$: 860.1995, found: 860.1979.

Imaging protocol

Patients were injected with up to 15 mCi (555 MBq; average 7.42 mCi [274.6 MBq], range 3.7–11.9 mCi [136.9–438.5 MBq]) ^{68}Ga-citrate intravenously. PET acquisition was acquired between 120 and 263 min after injection (average 210 min). Images were acquired on either a PET/CT or PET/magnetic resonance (MR). PET/CT examinations were performed on either a Biograph 16 (Hi-Rez) PET/CT scanner (Siemens AG) with an integrated PET and 16-MDCT scanner or a Discovery VCT PET/CT scanner (GE Medical Systems) with an integrated PET and 64-MDCT scanner. A low-dose CT was acquired for PET attenuation correction. PET/MR images were performed on a SIGNA PET/MR (GE Medical Systems). Attenuation correction for PET reconstruction was performed using a MR-based attenuation correction technique provided by the scanner manufacturer.

Image analysis

Maximum intensity projection, axial, coronal, and sagittal reconstructions and PET/MR fused images were reviewed on an

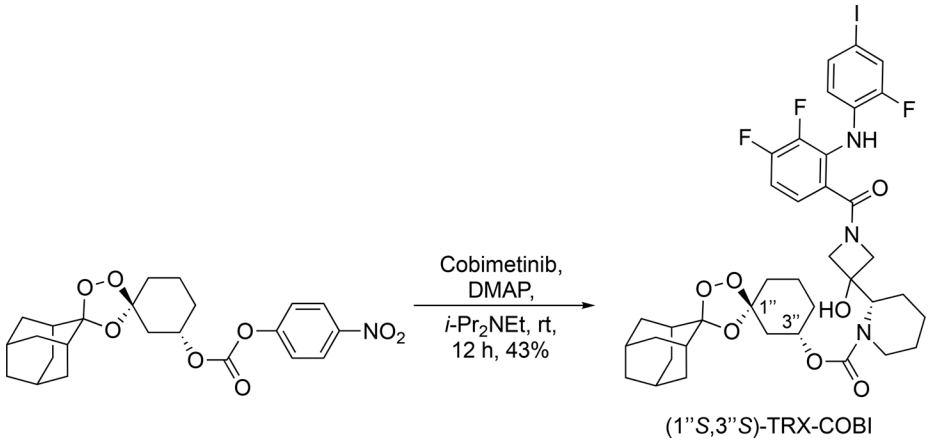

Scheme 2. (1"S,3"S)-dispiro[adamantane-2,3'-[1,2,4]trioxolane-5',1"-cyclohexan]-3"-yl(S)-2-(1-(3,4-difluoro-2-((2-fluoro-4-iodophenyl)amino)benzoyl)-3-hydroxyazetidin-3-yl)piperidine-1-carboxylate.

Advantage Windows workstation. PET images were evaluated by trained nuclear medicine physician blinded to the results of conventional imaging scans as well as clinical/genomic features of the case and scored for the presence of PET avid lesions. Lesions were considered PET positive if uptake was focal, greater than the adjacent background soft tissue and not in an expected physiologic structure such as the urinary bladder, vessels, or salivary glands.

For semiquantitative analysis, a volume of interest was manually drawn around PET avid lesions and SUV_{max} values (SUV, standardized uptake value) were recorded. The location of abnormal radiotracer uptake was compared to CT and nuclear medicine bone scans. Additionally, SUV_{mean} values were recorded in the liver, paraspinous soft tissues, bone (right sacrum), and mediastinal blood pool for the determination of normal structures.

With conventional imaging, soft tissue metastases were considered positive if >1 cm in long axis, except for lymph nodes that were considered positive if >1.5 cm in short axis. Bone lesions on radionuclide scan were considered positive if uptake was focal and not in a pattern consistent with arthritis or antecedent trauma/fracture.

Small animal PET/CT and biodistribution studies

6-wk-old male NSG mice were purchased from Jackson Laboratory. Mice were inoculated with 10^7 cells subcutaneously into one flank in a 1:1 mixture (vol/vol) of media and Matrigel. Tumors were palpable within 20 d after transplantation. ^{68}Ga-citrate was prepared by the radiopharmacy core facility at UCSF as previously reported (Behr et al., 2016). ^{18}F-TRX was prepared using the previously developed protocol. Radiotracers were administered via tail vein injection (150–250 µCi/mouse). Imaging data were acquired 4 h after injection of ^{68}Ga-citrate and 90 min after injection of ^{18}F-TRX. The image acquisition was performed on the Siemens Inveon micro-PET/CT under anesthesia by using 2.5% isoflurane at 4 h after injection. The resulting imaging data were directly reconstructed, decay corrected, and analyzed using AMIDE software, which was also used to place the region of interest to calculate SUV data from the static acquisition. After the imaging data were collected, animals were euthanized by cervical dislocation. Tissues were removed, weighed, and counted on a Hidex automatic gamma counter for accumulation activity. The mass of the injected radiotracer was measured and used to determine the total number of CPM by comparison with a standard of known activity. The data were background and decay corrected and expressed as the percentage of the injected dose/weight of the biospecimen in grams (%ID/g).

Orthotopic pancreas xenografts

Derivation of the p53 2.1.1 FVB/n mice has been described (Collisson et al., 2011). These cells were labeled *in vitro* with a lentiviral vector encoding a firefly luciferase to give rise p53 2.1.1syn_Luc. Overall, 1,000 cells were orthotopically implanted in 6-wk-old FVB/n mice in 20 µl composed 1:1 mixture (vol/vol) of media and Matrigel. Mice were treated with 7.5 mg/kg of COBI, 12 mg/kg TRX-COBI, or vehicle control (saline) by daily IP for 3 wk. Bioluminescent imaging was performed twice a week to monitor tumor growth.

KPT *lung tumor model*

Kras$^{LSL\text{-}G12D/+}$,*p53*$^{flox/flox}$,*R26*$^{LSL\text{-}tdTomato}$ (*KPT*) mice have been previously described. Mice were bred on a mixed background. Adenovirus-expressing Cre recombinase (Viraquest, University of Iowa) was administrated intratracheally as previously described (DuPage et al., 2009). Briefly, 2–3-mo-old mice were infected with 2×10^7 or 10^8 pfu of adenovirus-expressing Cre recombinase. After 40 d, 10 mg/kg of COBI, 16 mg/kg of TRX-COBI, or vehicle control (saline) were dosed by IP 5 d a week for 6 wk. Mice OS was analyzed, and images of tumors expressing tdTomato were acquired with a Zeiss AxioImager microscope.

PDXs

For generation of the PDX 260 model, informed consent was obtained from the patient as per an open IRB-approved protocol at UCSF. Tumors were implanted in NSG mice (Jackson Laboratory). TM00186 were obtained from Jackson Laboratory. Both tumors were used at low passage for the experiments described herein. In Fig. 4, once tumors reached an average volume of ∼300 mm^3, mice were treated with 7.5 mg/kg of COBI, 12 mg/kg TRX-COBI, or vehicle control (saline) by daily IP for 25 d. In Fig. 6, when tumors reached an average volume of ∼300 mm^3, animals were randomized into six groups as indicated. RMC-4550 was dosed by oral at 30 mg/kg. Measurement of tumor volume and body weight were performed twice a week.

TRX-PURO assay

Automated cell imaging was conducted using a GE IN Cell2000 automated cell imager. Graphing and analysis of data was performed in GraphPad Prism 6. A total of 3,000 cells per well were plated in 96-well black µClear tissue culture plates (Greiner). The following day, cells were incubated with a mixture of growth medium and adeno-Cre viral supernatant for 6 h. Cells were then exposed to puromycin or TRX-PURO at 1 µM (diluted in cell culture medium from 1,000× DMSO stocks) in medium for 24, 48, and 73 h before medium was removed and cells were washed with PBS, fixed in 4% paraformadehyde for 10 min at RT, and then washed twice with PBS and once with PBS containing 0.1% Triton X-100. Cells were then stained with Kerafast anti-puromycin antibody (3RH11; 1:500) in PBS with 10% FBS and 0.1% Triton X-100 for 30 min at 37°C. Cells were washed once with PBS and once with PBS containing 0.1% Triton X-100 and then stained with anti-mouse secondary FITC (488 nm excitation, 535 nm emission) antibody (1:100) and Hoechst nuclear stain at a final concentration of 10 µg/ml in PBS with 10% FBS and 0.1% Triton X-100 for 30 min at 37°C. Cells were washed once with PBS containing 0.1% Triton X-100 and once with PBS and then stored in PBS and imaged using an IN Cell 2000 automated cell imager at 10× magnification with six to nine images per well in FITC and DAPI channel fluorescence. Images were analyzed for nuclei count and puromycin incorporation using IN Cell Developer software. Puromycin incorporation was assessed by mean cellular fluorescence density in the FITC channel for each cell as defined by targets seeded with nuclei in the DAPI

channel. Average cellular fluorescence density under each condition was determined, and reported values represent the mean average per well across triplicates ±SEM. Signal in cells treated with the TRX-PURO was normalized to that in cells treated with free puromycin. These values were then normalized to untreated cells and reported at percent change from untreated.

Cell viability assays

3,000–5,000 cells optimized for each cell line were seeded on day 1, drug was added on day 2 (using DMSO normalized to 0.1%), and the cell viability was determined using CellTiter-glo (Promega) on day 4. Viability curves were generated using GraphPad Prism 6.

Histological analysis

H&E staining and immunohistochemistry were performed on 4-µm-thick sections of 4% paraformaldehyde-fixed and paraffin-embedded tissues. Tail sections were decalcified by incubation of trimmed paraffin blocks for 10–15 min on paper towels soaked in 1 N HCl. Epidermis thickness was measured using a Zeiss AxioImager microscope. Tumor sections were stained with phospho-p44/42 (Thr202/Tyr204, 9,101, 1:50).

PRISM screening

Cancer cell line profiling was performed using the PRISM platform, as previously described (Hensley et al., 2016). Cell treatment and data analysis were performed as described in https://depmap.org/ repurposing. Raw Luminex signal was converted to EC_{50} values for each cell line.

Detection of labile ferrous iron

Cells were seeded and cultured overnight. Culture medium was removed on the following day rinse twice gently with PBS. A final concentration of 5 µM of SiRhoNox (GORYO Chemical; FerroFarRed) in a serum-free culture medium was added to the dish and incubated for 1 h at 37°C.

Fluorescence images were then acquired with a Zeiss spinning-disk confocal microscope. Immunofluorescence was quantified using ImageJ software.

Pharmacokinetic assays

NSG mice were administered a single IP dose of COBI (7.5 mg/kg, $n = 3$) or TRX-COBI (12 mg/kg, $n = 3$). Blood, tumor, liver, and spleen were collected after 7 h and analyzed by Integrated Analytical Solutions, Inc.

Western blotting

Tumor tissue and organ tissues were flash frozen in liquid nitrogen and homogenized in M-PER lysis buffer (Thermo Fisher Scientific) plus Halt protease and phosphatase inhibitor cocktail (Thermo Fisher Scientific). Protein concentrations were determined with the Pierce BCA protein assay kit (Thermo Fisher Scientific), extracts were loaded onto NuPAGE Bis–Tris SDS gels, and immunoblots were visualized using a LiCOR Odyssey system.

STEAP3 *knockdown*

For stable and lentivirally transfected shRNA-based knockdown experiments, viruses were generated in HEK293T cells transfected with lentiviral packaging vectors along with vectors expressing pGIPZ-shSTEAP3 using Fugene6 (Promega). Two distinct hairpins were chosen for the experiments. Their sequences are as follows: STEAP3-1, 5′-TGAAGAACTTGTTCTGGCT; STEAP3-2, 5′-TGACCACTGTGCAAGTGGG-3′. Viral supernatant collected from confluent monoculture was filtered and used to infect MiaPaca-2 and Capan1 pancreatic cancer cells. A total of 0.5×10^6 cells were seeded in one well of a 6-well chamber and allowed to grow for overnight. The following day, cells were incubated with a 1:2 mixture of growth medium and viral supernatant collected from HEK293T cells. Polybrene was added at 8 µg ml/liter.

Quantification and statistical analysis

Statistical tests were performed using GraphPad Prism 7.0 or the R language. A two-sided two-sample *t*-test was used for comparisons of the means of data between two groups. One-way ANOVA was used for comparisons among multiple independent groups. The Cox proportional hazards model was used to assess OS, while the Kaplan–Meier method was used to visualize STEAP3 expression when stratified into high versus low. For animal studies, animals were randomized before treatments, and all animals treated were included for the analyses.

Online supplemental material

Fig. S1 shows how oncogenic KRAS elevates and maintains the ferrous iron pool. Fig. S2 shows how TRX-COBI acts through ferrous iron–mediated payload (COBI) release and resultant MEK inhibition. Fig. S3 shows how TRX-COBI spares skin toxicity. Fig. S4 shows how FeADC-based MEK inhibition is tolerable in vivo and less toxic to normal cells. Table S1 lists stability of (1″*R*, 3″*R*)-TRX-COBI and (1″*S*, 3″*S*)-TRX-COBI conjugates in mouse liver microsomes (MLMs). Table S2 lists pharmacokinetic parameters for (1″*R*, 3″*R*)-TRX-COBI and (released) COBI following a single 15 mg/kg IP dose of (1″*R*, 3″*R*)-TRX-COBI to NSG mice. Table S3 lists key resources used in this study. Data S1 contains scans of NMR, HMRS spectra, and LCMS chromatograms.

Acknowledgments

We thank Bob Nichols, Mallika Singh, Rushika Perera, and Trever Bivona for their scientific advice and comments. We also thank the Preclinical Therapeutics Core and the Laboratory for Cell Analysis core at UCSF Helen Diller Comprehensive Cancer Center.

This work was supported by National Institutes of Health (NIH), National Cancer Institute grants R01 (CA178015, CA222862, CA227807, CA239604, CA230263), and U24 (CA210974); NIH grant P30CA082103 (A.B. Olshen); NIH (AI105106) and Congressionally Directed Medical Research Program (W81XWH1810763 and W81XWH1810754) grants (A.R. Renslo); American Cancer Society Research Scholar grant 130635-RSG-17-005-01-CCE (M.J. Evans); and the Shorenstein, Rhombauer, and Preston Families. Content does not reflect the views of the funders.

Author contributions: Conception and design: H. Jiang, E.A. Collisson, and A.R. Renslo. Development of methodology: H. Jiang, R.K. Muir, E.A. Collisson, and A.R. Renslo. Data

acquisition: H. Jiang, R.K. Muir, R.L. Gonciarz, J.E. Korkola, E.A. Collisson, and A.R. Renslo. Analysis and interpretation of data: H. Jiang, R.K. Muir, R.L. Gonciarz, A.B. Olshen, I. Yeh, B.C. Hann, N. Zhao, Y. Wang, S.C. Behr, M.J. Evans, E.A. Collisson, and A.R. Renslo. Writing and review of the manuscript: H. Jiang, E.A. Collisson, and A.R. Renslo. Study supervision: E.A. Collisson and A.R. Renslo.

Disclosures: R.K. Muir reported a patent to WO2019/005977 issued. S.C. Behr reported grants from CTT, and personal fees from AAA Novartis and Genvivo outside the submitted work. J. Korkola reported "other" from Convergent Genomics outside the submitted work. M.J. Evans reported a patent to Trioxolane Agents (PCT/US2018/039768) pending. E.A. Collisson reported grants from Astra Zeneca and Bayer outside the submitted work. E.A. Collisson and A.R. Renslo are cofounders of Tatara and have an ownership interest in the company. A.R. Renslo reported personal fees from Tatara Therapeutics outside the submitted work; in addition, A.R. Renslo had a patent number 10,287,312 issued, a patent number 10,662,215 issued, a patent number 11,014,955 issued, and a patent number 11,072,594 issued. No other disclosures were reported.

Submitted: 2 April 2021
Revised: 2 August 2021
Accepted: 1 November 2021

References

Adjei, A.A., R.B. Cohen, W. Franklin, C. Morris, D. Wilson, J.R. Molina, L.J. Hanson, L. Gore, L. Chow, S. Leong, et al. 2008. Phase I pharmacokinetic and pharmacodynamic study of the oral, small-molecule mitogen-activated protein kinase kinase 1/2 inhibitor AZD6244 (ARRY-142886) in patients with advanced cancers. *J. Clin. Oncol.* 26:2139–2146. https://doi.org/10.1200/jco.2007.14.4956

Aguirre, A.J., J.A. Nowak, N.D. Camarda, R.A. Moffitt, A.A. Ghazani, M. Hazar-Rethinam, S. Raghavan, J. Kim, L.K. Brais, D. Ragon, et al. 2018. Real-time genomic characterization of advanced pancreatic cancer to enable precision medicine. *Cancer Discov.* 8:1096–1111. https://doi.org/10.1158/2159-8290.CD-18-0275

Ansari, M.T., Z.S. Saify, N. Sultana, I. Ahmad, S. Saeed-Ul-Hassan, I. Tariq, and M .Khanum. 2013. Malaria and artemisinin derivatives: An updated review. *Mini Rev. Med. Chem.* 13:1879–1902. https://doi.org/10.2174/13895575113136660097

Aron, A.T., A.G. Reeves, and C.J. Chang. 2018. Activity-based sensing fluorescent probes for iron in biological systems. *Curr. Opin. Chem. Biol.* 43: 113–118. https://doi.org/10.1016/j.cbpa.2017.12.010

Azan, A., P.J. Caspers, T.C. Bakker Schut, S. Roy, C. Boutros, C. Mateus, E. Routier, B. Besse, D. Planchard, A. Seck, et al. 2017. A novel spectroscopically determined pharmacodynamic biomarker for skin toxicity in cancer patients treated with targeted agents. *Cancer Res.* 77:557–565. https://doi.org/10.1158/0008-5472.CAN-16-1733

Balagula, Y., K. Barth Huston, K.J. Busam, M.E. Lacouture, P.B. Chapman, and P.L. Myskowski. 2011. Dermatologic side effects associated with the MEK 1/2 inhibitor selumetinib (AZD6244, ARRY-142886). *Invest New Drugs.* 29:1114–1121. https://doi.org/10.1007/s10637-010-9567-3

Behr, S.C., R. Aggarwal, Y. Seo, C.M. Aparici, E. Chang, K.T. Gao, D.H. Tao, E.J. Small, and M.J Evans. 2016. A feasibility study showing [(68)Ga]citrate PET detects prostate cancer. *Mol. Imaging Biol.* 18:946–951. https://doi.org/10.1007/s11307-016-0966-5

Behr, S.C., J.E. Villanueva-Meyer, Y. Li, Y.H. Wang, J. Wei, A. Moroz, J.K. Lee, J.C. Hsiao, K.T. Gao, W. Ma, et al. 2018. Targeting iron metabolism in high-grade glioma with 68Ga-citrate PET/MR. *JCI Insight.* 3. e. https://doi.org/10.1172/jci.insight.93999

Bersuker, K., J.M. Hendricks, Z. Li, L. Magtanong, B. Ford, P.H. Tang, M.A. Roberts, B. Tong, T.J. Maimone, R. Zoncu, et al. 2019. The CoQ oxidoreductase FSP1 acts parallel to GPX4 to inhibit ferroptosis. *Nature.* 575:688–692. https://doi.org/10.1038/s41586-019-1705-2

Blank, B.R., R.L. Gonciarz, P. Talukder, J. Gut, J. Legac, P.J. Rosenthal, and A.R Renslo. 2020. Antimalarial trioxolanes with superior drug-like properties and in vivo efficacy. *ACS Infect. Dis.* 6:1827–1835. https://doi.org/10.1021/acsinfecdis.0c00064

Brady, D.C., M.S. Crowe, M.L. Turski, G.A. Hobbs, X. Yao, A. Chaikuad, S. Knapp, K. Xiao, S.L. Campbell, D.J. Thiele, et al. 2014. Copper is required for oncogenic BRAF signalling and tumorigenesis. *Nature.* 509:492–496. https://doi.org/10.1038/nature13180

Bruemmer, K.J., S.W.M. Crossley, and C.J Chang. 2020. Activity-based sensing: A synthetic methods approach for selective molecular imaging and beyond. *Angew. Chem. Int. Ed. Engl.* 59:13734–13762. https://doi.org/10.1002/anie.201909690

Burgess, M.R., E. Hwang, R. Mroue, C.M. Bielski, A.M. Wandler, B.J. Huang, A.J. Firestone, A. Young, J.A. Lacap, L. Crocker, et al. 2017. KRAS allelic imbalance enhances fitness and modulates MAP kinase dependence in cancer. *Cell.* 168:817–829.e15. https://doi.org/10.1016/j.cell.2017.01.020

Buss, J.L., F.M. Torti, and S.V Torti. 2003. The role of iron chelation in cancer therapy. *Curr. Med. Chem.* 10:1021–1034. https://doi.org/10.2174/0929867033457638

Chang, C.J. 2015. Searching for harmony in transition-metal signaling. *Nat. Chem. Biol.* 11:744–747. https://doi.org/10.1038/nchembio.1913

Choo, E.F., M. Belvin, J. Boggs, Y. Deng, K.P. Hoeflich, J. Ly, M. Merchant, C. Orr, E. Plise, K. Robarge, et al. 2012. Preclinical disposition of GDC-0973 and prospective and retrospective analysis of human dose and efficacy predictions. *Drug Metab. Dispos.* 40:919–927. https://doi.org/10.1124/dmd.111.043778

Chung, C.Y., J.M. Posimo, S. Lee, T. Tsang, J.M. Davis, D.C. Brady, and C.J Chang. 2019. Activity-based ratiometric FRET probe reveals oncogene-driven changes in labile copper pools induced by altered glutathione metabolism. *Proc. Natl. Acad. Sci. USA.* 116:18285–18294. https://doi.org/10.1073/pnas.1904610116

Collisson, E.A., A. Sadanandam, P. Olson, W.J. Gibb, M. Truitt, S. Gu, J. Cooc, J. Weinkle, G.E. Kim, L. Jakkula, et al. 2011. Subtypes of pancreatic ductal adenocarcinoma and their differing responses to therapy. *Nat. Med.* 17: 500–503. https://doi.org/10.1038/nm.2344

Collisson, E.A., C.L. Trejo, J.M. Silva, S. Gu, J.E. Korkola, L.M. Heiser, R.P. Charles, B.A. Rabinovich, B. Hann, D. Dankort, et al. 2012. A central role for RAF->MEK->ERK signaling in the genesis of pancreatic ductal adenocarcinoma. *Cancer Discov.* 2:685–693. https://doi.org/10.1158/2159-8290.CD-11-0347

Corna, G., L. Campana, E. Pignatti, A. Castiglioni, E. Tagliafico, L. Bosurgi, A. Campanella, S. Brunelli, A.A. Manfredi, P. Apostoli, et al. 2010. Polarization dictates iron handling by inflammatory and alternatively activated macrophages. *Haematologica.* 95:1814–1822. https://doi.org/10.3324/haematol.2010.023879

Danilenko, D.M., G.D. Phillips, and D. Diaz. 2016. In vitro skin models and their predictability in defining normal and disease biology, pharmacology, and toxicity. *Toxicol. Pathol.* 44:555–563. https://doi.org/10.1177/0192623316632074

Ding, H., A. Blair, Y. Yang, and J.M. Stuart. 2019. Biological process activity transformation of single cell gene expression for cross-species alignment. *Nat. Commun.* 10:4899. https://doi.org/10.1038/s41467-019-12924-w

Dixon, S.J., K.M. Lemberg, M.R. Lamprecht, R. Skouta, E.M. Zaitsev, C.E. Gleason, D.N. Patel, A.J. Bauer, A.M. Cantley, W.S. Yang, et al. 2012. Ferroptosis: An iron-dependent form of nonapoptotic cell death. *Cell.* 149:1060–1072. https://doi.org/10.1016/j.cell.2012.03.042

Dixon, S.J., and B.R. Stockwell. 2014. The role of iron and reactive oxygen species in cell death. *Nat. Chem. Biol.* 10:9–17. https://doi.org/10.1038/nchembio.1416

Doll, S., F.P. Freitas, R. Shah, M. Aldrovandi, M.C. da Silva, I. Ingold, A.G. Grocin, T.N. Xavier da Silva, E. Panzilius, C.H. Scheel, et al. 2019. FSP1 is a glutathione-independent ferroptosis suppressor. *Nature.* 575:693–698. https://doi.org/10.1038/s41586-019-1707-0

DuPage, M., A.L. Dooley, and T. Jacks. 2009. Conditional mouse lung cancer models using adenoviral or lentiviral delivery of Cre recombinase. *Nat. Protoc.* 4:1064–1072. https://doi.org/10.1038/nprot.2009.95

Fedele, C., H. Ran, B. Diskin, W. Wei, J. Jen, M.J. Geer, K. Araki, U. Ozerdem, D.M. Simeone, G. Miller, et al. 2018. SHP2 inhibition prevents adaptive resistance to MEK inhibitors in multiple cancer models. *Cancer Discov.* 8: 1237–1249. https://doi.org/10.1158/2159-8290.CD-18-0444

Fontaine, S.D., A.G. DiPasquale, and A.R. Renslo. 2014. Efficient and stereocontrolled synthesis of 1,2,4-trioxolanes useful for ferrous iron-

dependent drug delivery. *Org. Lett.* 16:5776–5779. https://doi.org/10.1021/ol5028392

Forcina, G.C., and S.J. Dixon. 2019. GPX4 at the crossroads of lipid homeostasis and ferroptosis. *Proteomics*. 19:e1800311. https://doi.org/10.1002/pmic.201800311

Han, M., R. Xu, S. Wang, N. Yang, S. Ni, Q. Zhang, Y. Xu, X. Zhang, C. Zhang, Y. Wei, et al. 2018. Six-transmembrane epithelial antigen of prostate 3 predicts poor prognosis and promotes glioblastoma growth and invasion. *Neoplasia*. 20:543–554. https://doi.org/10.1016/j.neo.2018.04.002

Hangauer, M.J., V.S. Viswanathan, M.J. Ryan, D. Bole, J.K. Eaton, A. Matov, J. Galeas, H.D. Dhruv, M.E. Berens, S.L. Schreiber, et al. 2017. Drug-tolerant persister cancer cells are vulnerable to GPX4 inhibition. *Nature*. 551:247–250. https://doi.org/10.1038/nature24297

Hensley, C.T., B. Faubert, Q. Yuan, N. Lev-Cohain, E. Jin, J. Kim, L. Jiang, B. Ko, R. Skelton, L. Loudat, et al. 2016. Metabolic heterogeneity in human lung tumors. *Cell*. 164:681–694. https://doi.org/10.1016/j.cell.2015.12.034

Hirayama, T. 2019. Fluorescent probes for the detection of catalytic Fe(II) ion. *Free Radic. Biol. Med.* 133:38–45. https://doi.org/10.1016/j.freeradbiomed.2018.07.004

Hirayama, T., M. Inden, H. Tsuboi, M. Niwa, Y. Uchida, Y. Naka, I. Hozumi, and H. Nagasawa. 2019. A Golgi-targeting fluorescent probe for labile Fe(II) to reveal an abnormal cellular iron distribution induced by dysfunction of VPS35. *Chem. Sci.* 10:1514–1521. https://doi.org/10.1039/c8sc04386h

Hirayama, T., H. Tsuboi, M. Niwa, A. Miki, S. Kadota, Y. Ikeshita, K. Okuda, and H. Nagasawa. 2017. A universal fluorogenic switch for Fe(II) ion based on N-oxide chemistry permits the visualization of intracellular redox equilibrium shift towards labile iron in hypoxic tumor cells. *Chem. Sci.* 8:4858–4866. https://doi.org/10.1039/c6sc05457a

Infante, J.R., L.A. Fecher, G.S. Falchook, S. Nallapareddy, M.S. Gordon, C. Becerra, D.J. DeMarini, D.S. Cox, Y. Xu, S.R. Morris, et al. 2012. Safety, pharmacokinetic, pharmacodynamic, and efficacy data for the oral MEK inhibitor trametinib: A phase 1 dose-escalation trial. *Lancet Oncol.* 13:773–781. https://doi.org/10.1016/S1470-2045(12)70270-X

Jackson, E.L., N. Willis, K. Mercer, R.T. Bronson, D. Crowley, R. Montoya, T. Jacks, and D.A. Tuveson. 2001. Analysis of lung tumor initiation and progression using conditional expression of oncogenic K-ras. *Genes Dev.* 15:3243–3248. https://doi.org/10.1101/gad.943001

Kakhlon, O., Y. Gruenbaum, and Z.I. Cabantchik. 2002. Ferritin expression modulates cell cycle dynamics and cell responsiveness to H-ras-induced growth via expansion of the labile iron pool. *Biochem. J.* 363:431–436. https://doi.org/10.1042/0264-6021:3630431

Karreth, F.A., K.K. Frese, G.M. Denicola, M. Baccarini, and D.A. Tuveson. 2011. C-Raf is required for the initiation of lung cancer by K-Ras(G12D). *Cancer Discov.* 1:128–136. https://doi.org/10.1158/2159-8290.CD-10-0044

Khan, M., and S. Gasser. 2016. Generating primary fibroblast cultures from mouse ear and tail tissues. *J. Vis. Exp.* 10:53565. https://doi.org/10.3791/53565

Kim, D., J.Y. Xue, and P. Lito. 2020. Targeting KRAS(G12C): From inhibitory mechanism to modulation of antitumor effects in patients. *Cell*. 183:850–859. https://doi.org/10.1016/j.cell.2020.09.044

Ko, A.H., T. Bekaii-Saab, J. Van Ziffle, O.M. Mirzoeva, N.M. Joseph, A. Talasaz, P. Kuhn, M.A. Tempero, E.A. Collisson, R.K. Kelley, et al. 2016. A multicenter, open-label phase II clinical trial of combined MEK plus EGFR inhibition for chemotherapy-refractory advanced pancreatic adenocarcinoma. *Clin. Cancer Res.* 22:61–68. https://doi.org/10.1158/1078-0432.CCR-15-0979

Larson, S.M., J.S. Rasey, D.R. Allen, N.J. Nelson, Z. Grunbaum, G.D. Harp, and D.L Williams. 1980. Common pathway for tumor cell uptake of gallium-67 and iron-59 via a transferrin receptor. *J. Natl. Cancer Inst.* 64:41–53

Liu, H., S.L. Schreiber, and B.R Stockwell. 2018. Targeting dependency on the GPX4 lipid peroxide repair pathway for cancer therapy. *Biochemistry*. 57:2059–2060. https://doi.org/10.1021/acs.biochem.8b00307

Mahajan, S.S., J. Gut, P.J. Rosenthal, and A.R Renslo. 2012. Ferrous iron-dependent delivery of therapeutic agents to the malaria parasite. *Future Med. Chem.* 4:2241–2249. https://doi.org/10.4155/fmc.12.174

Miller, L.D., L.G. Coffman, J.W. Chou, M.A. Black, J. Bergh, R. D'Agostino Jr., S.V. Torti, and F.M. Torti. 2011. An iron regulatory gene signature predicts outcome in breast cancer. *Cancer Res.* 71:6728–6737. https://doi.org/10.1158/0008-5472.CAN-11-1870

Muir, R.K., N. Zhao, J. Wei, Y.H. Wang, A. Moroz, Y. Huang, Y.C. Chen, R. Sriram, J. Kurhanewicz, D. Ruggero, et al. 2019. Measuring dynamic changes in the labile iron pool in vivo with a reactivity-based probe for positron emission tomography. *ACS Cent. Sci.* 5:727–736. https://doi.org/10.1021/acscentsci.9b00240

O'Neill, P.M., and G.H. Posner. 2004. A medicinal chemistry perspective on artemisinin and related endoperoxides. *J. Med. Chem.* 47:2945–2964. https://doi.org/10.1021/jm030571c

Papke, B., and C.J. Der. 2017. Drugging RAS: Know the enemy. *Science*. 355:1158–1163. https://doi.org/10.1126/science.aam7622

Perera, R.M., and N. Bardeesy. 2015. Pancreatic cancer metabolism: Breaking it down to build it back up. *Cancer Discov.* 5:1247–1261. https://doi.org/10.1158/2159-8290.CD-15-0671

Pinnix, Z.K., L.D. Miller, W. Wang, R. D'Agostino, Jr., T. Kute, M.C. Willingham, H. Hatcher, L. Tesfay, G. Sui, X. Di, et al. 2010. Ferroportin and iron regulation in breast cancer progression and prognosis. *Sci. Transl Med.* 2:43ra56. https://doi.org/10.1126/scitranslmed.3001127

Recalcati, S., M. Locati, A. Marini, P. Santambrogio, F. Zaninotto, M. De Pizzol, L. Zammataro, D. Girelli, and G. Cairo. 2010. Differential regulation of iron homeostasis during human macrophage polarized activation. *Eur. J. Immunol.* 40:824–835. https://doi.org/10.1002/eji.200939889

Reichert, M., S. Takano, S. Heeg, B. Bakir, G.P. Botta, and A.K Rustgi. 2013. Isolation, culture and genetic manipulation of mouse pancreatic ductal cells. *Nat. Protoc.* 8:1354–1365. https://doi.org/10.1038/nprot.2013.079

Ruess, D.A., G.J. Heynen, K.J. Ciecielski, J. Ai, A. Berninger, D. Kabacaoglu, K. Gorgulu, Z. Dantes, S.M. Wormann, K.N. Diakopoulos, et al. 2018. Mutant KRAS-driven cancers depend on PTPN11/SHP2 phosphatase. *Nat. Med.* 24:954–960. https://doi.org/10.1038/s41591-018-0024-8

Saunders, I.M., A.M. Goodman, and R. Kurzrock. 2020. Real-world toxicity experience with BRAF/MEK inhibitors in patients with Erdheim-Chester disease. *Oncologist*. 25:e386–e390. https://doi.org/10.1634/theoncologist.2019-0606

Scholl, F.A., P.A. Dumesic, D.I. Barragan, K. Harada, J. Charron, and P.A. Khavari. 2009. Selective role for Mek1 but not Mek2 in the induction of epidermal neoplasia. *Cancer Res.* 69:3772–3778. https://doi.org/10.1158/0008-5472.can-08-1963

Schonberg, D.L., T.E. Miller, Q. Wu, W.A. Flavahan, N.K. Das, J.S. Hale, C.G. Hubert, S.C. Mack, A.M. Jarrar, R.T. Karl, et al. 2015. Preferential iron trafficking characterizes glioblastoma Stem-like cells. *Cancer Cell*. 28:441–455. https://doi.org/10.1016/j.ccell.2015.09.002

Serrano, M., A.W. Lin, M.E. McCurrach, D. Beach, and S.W. Lowe. 1997. Oncogenic ras provokes premature cell senescence associated with accumulation of p53 and p16INK4a. *Cell*. 88:593–602. https://doi.org/10.1016/s0092-8674(00)81902-9

Seton-Rogers, S. 2020. KRAS-G12C in the crosshairs. *Nat. Rev. Cancer*. 20:3. https://doi.org/10.1038/s41568-019-0228-3

Siegel, R.L., K.D. Miller, and A. Jemal. 2018. Cancer statistics, 2018. *CA Cancer J. Clin.* 68:7–30. https://doi.org/10.3322/caac.21442

Spangler, B., S.D. Fontaine, Y. Shi, L. Sambucetti, A.N. Mattis, B. Hann, J.A. Wells, and A.R. Renslo. 2016a. A novel tumor-activated prodrug strategy targeting ferrous iron is effective in multiple preclinical cancer models. *J. Med. Chem.* 59:11161–11170. https://doi.org/10.1021/acs.jmedchem.6b01470

Spangler, B., C.W. Morgan, S.D. Fontaine, M.N. Vander Wal, C.J. Chang, J.A. Wells, and A.R Renslo. 2016b. A reactivity-based probe of the intracellular labile ferrous iron pool. *Nat. Chem. Biol.* 12:680–685. https://doi.org/10.1038/nchembio.2116

Stephen, A.G., D. Esposito, R.K. Bagni, and F. McCormick. 2014. Dragging ras back in the ring. *Cancer Cell*. 25:272–281. https://doi.org/10.1016/j.ccr.2014.02.017

Stockwell, B.R., J.P. Friedmann Angeli, H. Bayir, A.I. Bush, M. Conrad, S.J. Dixon, S. Fulda, S. Gascon, S.K. Hatzios, V.E. Kagan, et al. 2017. Ferroptosis: A regulated cell death Nexus linking metabolism, redox biology, and disease. *Cell*. 171:273–285. https://doi.org/10.1016/j.cell.2017.09.021

Tesfay, L., K.A. Clausen, J.W. Kim, P. Hegde, X. Wang, L.D. Miller, Z. Deng, N. Blanchette, T. Arvedson, C.K. Miranti, et al. 2015. Hepcidin regulation in prostate and its disruption in prostate cancer. *Cancer Res.* 75:2254–2263. https://doi.org/10.1158/0008-5472.CAN-14-2465

Torti, S.V., and F.M. Torti. 2013a. Cellular iron metabolism in prognosis and therapy of breast cancer. *Crit. Rev. Oncog.* 18:435–448. https://doi.org/10.1615/critrevoncog.2013007784

Torti, S.V., and F.M. Torti. 2013b. Iron and cancer: More ore to be mined. *Nat. Rev. Cancer*. 13:342–355. https://doi.org/10.1038/nrc3495

Weber, R.A., F.S. Yen, S.P.V. Nicholson, H. Alwaseem, E.C. Bayraktar, M. Alam, R.C. Timson, K. La, M. Abu-Remaileh, H. Molina, et al. 2020. Maintaining iron homeostasis is the key role of lysosomal acidity for cell proliferation. *Mol. Cell*. 77:645–655.e7. https://doi.org/10.1016/j.molcel.2020.01.003

Ying, H., A.C. Kimmelman, C.A. Lyssiotis, S. Hua, G.C. Chu, E. Fletcher-Sananikone, J.W. Locasale, J. Son, H. Zhang, J.L. Coloff, et al. 2012.

Oncogenic Kras maintains pancreatic tumors through regulation of anabolic glucose metabolism. *Cell*. 149:656–670. https://doi.org/10.1016/j.cell.2012.01.058

Yu, C., A.M. Mannan, G.M. Yvone, K.N. Ross, Y.L. Zhang, M.A. Marton, B.R. Taylor, A. Crenshaw, J.Z. Gould, P. Tamayo, et al. 2016. High-throughput identification of genotype-specific cancer vulnerabilities in mixtures of barcoded tumor cell lines. *Nat. Biotechnol.* 34:419–423. https://doi.org/10.1038/nbt.3460

Zhao, N., Y. Huang, Y.H. Wang, R.K. Muir, Y.C. Chen, J. Wei, N. Hooshdaran, P. Viswanath, Y. Seo, D. Ruggero, et al. 2021. Ferronostics: Measuring tumoral ferrous iron with PET to predict sensitivity to iron-targeted cancer therapies. *J. Nucl. Med.* 62:949–955. https://doi.org/10.2967/jnumed.120.252460

Zhao, Y., and A.A. Adjei. 2014. The clinical development of MEK inhibitors. *Nat. Rev. Clin. Oncol.* 11:385–400. https://doi.org/10.1038/nrclinonc.2014.83

Supplemental material

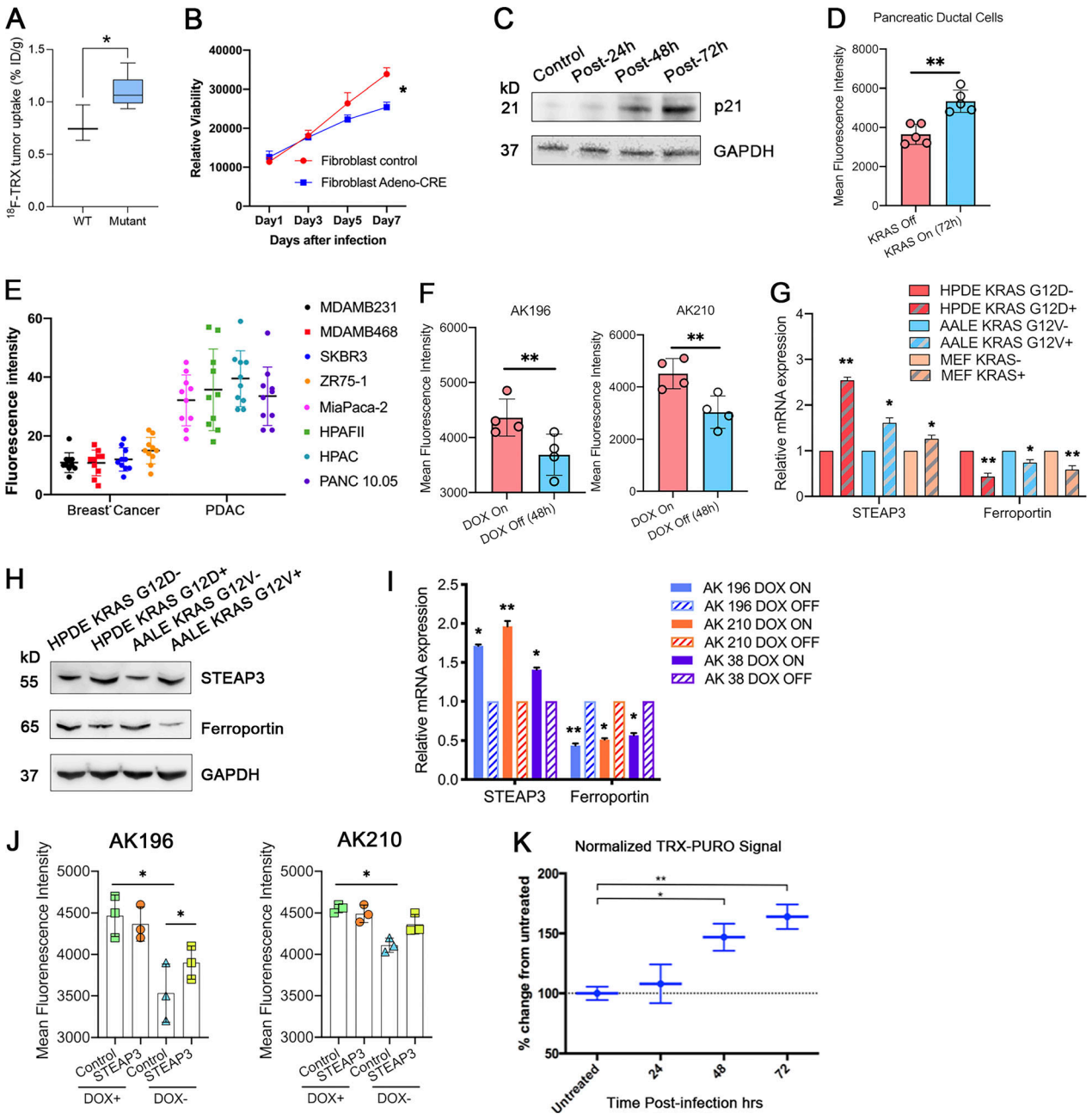

Figure S1. **Oncogenic KRAS elevates and maintains the ferrous iron pool. (A)** ^{18}F-TRX uptake in mice bearing xenografts with wild-type or mutant KRAS. Error bars represent mean ± SEM, *n* = 3 mice/group and analyzed by a two-sample *t*-test. *, P < 0.05. **(B)** Proliferation curve of *LSL-Kras^{G12D}* fibroblasts with or without AdCre treatment. **(C)** Western blot for p21 of *LSL-Kras^{G12D}* fibroblasts before and after the treatment with AdCre at 24, 48, and 72 h. **(D)** Quantification of the fluorescent intensity for Fig. 2 D. Error bars represent mean ± SEM, analyzed by a two-sample *t*-test. **, P < 0.01. **(E)** Quantifications of the fluorescence intensity stained with SiRhoNox in various breast and pancreatic cancer cell lines. **(F)** Quantification of the fluorescent intensity of SiRhoNox by flow cytometry in *iKras* cells treated with or without doxycycline. Error bars represent mean ± SEM, analyzed by a two-sample *t*-test. **, P < 0.01. **(G)** Quantitative PCR analysis of STEAP3 and ferroportin expression in indicated cells. Error bars represent mean ± SEM and analyzed by one-way ANOVA and shown as *, P < 0.05; **, P < 0.01. **(H)** Western blot for STEAP3 and ferroportin in HPDE, HPDE *KRAS^{G12D}* cells, and AALE and AALE *KRAS^{G12V}* cells. **(I)** Quantitative PCR analysis of *Steap3* and *Fpn* (ferroportin) in *iKras* cells treated with or without doxycycline. Error bars represent mean ± SEM and analyzed by one-way ANOVA and shown as *, P < 0.05; **, P < 0.01. **(J)** Quantification of the fluorescent intensity of SiRhoNox by flow cytometry in control or STEAP3-overexpressed *iKras* cells treated with or without doxycycline. Error bars represent mean ± SEM, analyzed by a two-sample *t*-test. *, P < 0.05. **(K)** Normalized TRX-PURO signals in *LSL-Kras^{G12D}* mouse fibroblasts before and after the treatment with AdCre at 24, 48, and 72 h. Each panel in E–G is representative of at least two independent experiments.

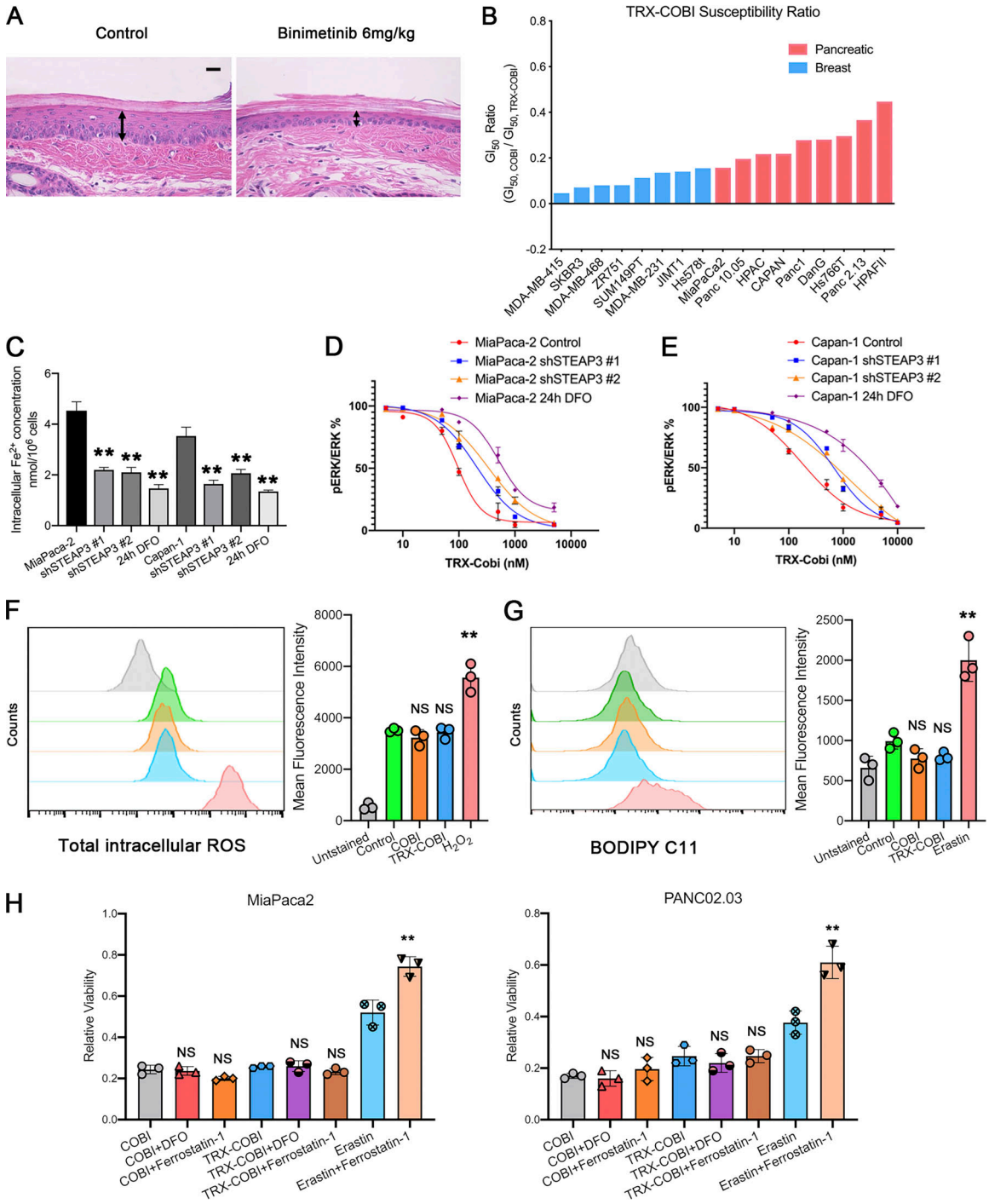

Figure S2. **TRX-COBI acts through ferrous iron–mediated payload (COBI) release and resultant MEK inhibition. (A)** Representative images of H&E (40×) showing the epidermal layer of mouse tail skin after treatment with vehicle or binimetinib for 20 d. The representative image of vehicle is the same as in Fig. 5 E. Scale bar: 20 µm. **(B)** Sensitivity of pancreatic and breast cancer cells to TRX-COBI expressed as a GI_{50} ratio, defined as the GI_{50} COBI divided by the GI_{50} of TRX-COBI. Cells were treated for 5 d. **(C)** Quantification of intracellular Fe^{2+} levels measured by SiRhoNox in MiaPaca2 and Capan-1 cells with STEAP3 knockdown and iron chelator DFO treatment. **(D and E)** Phospho-ERK/total ERK levels in MiaPaca2 and Capan-1 cells with STEAP3 knockdown or after 24 h of DFO (iron chelator) treatment. Cells were treated with the indicated concentration of TRX-COBI for 2 h before lysis. Error bars indicate ±SD. **(F)** ROS production in MiaPaca2 cells assessed by flow cytometry after cells were incubated with vehicle (DMSO), COBI (100 nM for 6 h), TRX-COBI (100 nM for 6 h), or H_2O_2 (50 µM for 1 h). Quantification for the fluorescent intensity. Error bars represent mean ± SEM, analyzed by a two-sample *t*-test. **, P < 0.01. **(G)** Lipid peroxidation in MiaPaca2 cells as assessed by flow cytometry using C11 BODIPY after cells were incubated with either vehicle (DMSO), COBI (100 nM, 10 h), TRX-COBI (100 nM, 10 h), or the ferroptosis inducer erastin (10 µM for 10 h). Quantification for the fluorescent intensity. Error bars represent mean ± SEM, analyzed by a two-sample *t*-test. **, P < 0.01. **(H)** Cell viability was measured after 24 h incubation in MiaPaca2 and PANC02.03 cells. Cells were incubated with single-agent COBI (100 nM), or single-agent TRX-COBI (100 nM) or erastin (10 µM), or cotreatments including COBI + DFO (100 µM), COBI + ferrostatin-1 (1 µM), TRX-COBI + DFO (100 µM), TRX-COBI + ferrostatin-1 (1 µM), or erastin + ferrostatin-1 (1 µM). Error bars represent mean ± SEM, analyzed by a two-sample *t*-test. **, P < 0.01. Each panel in F and G is representative of three independent experiments.

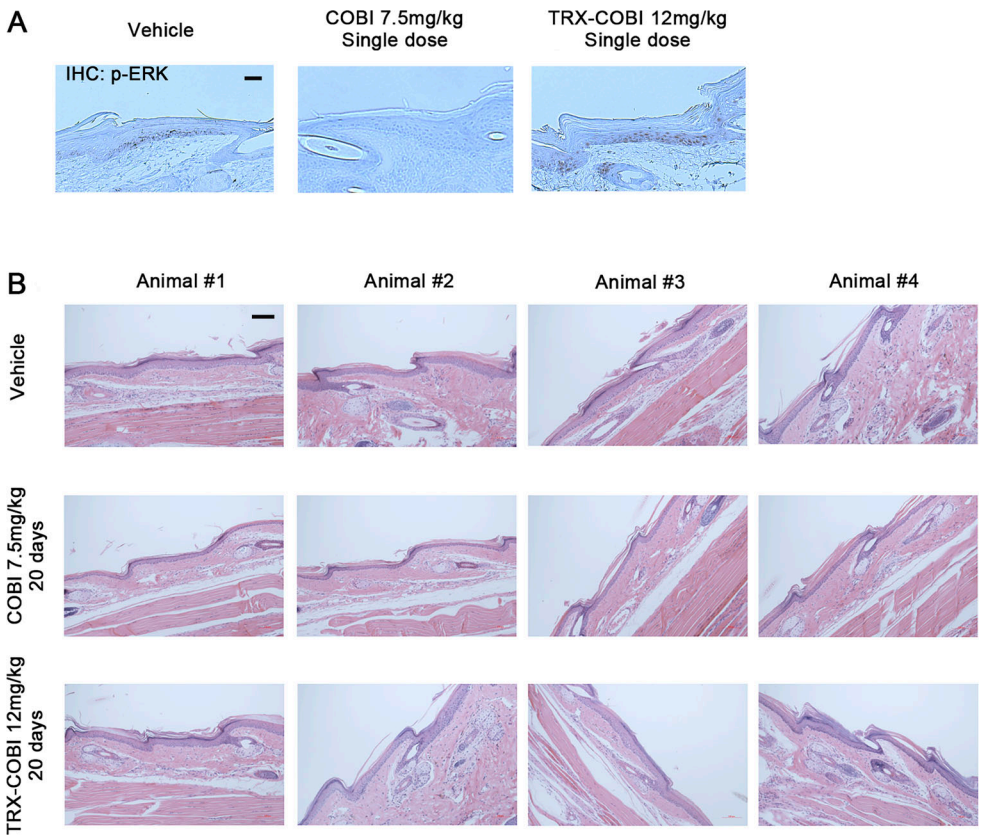

Figure S3. **TRX-COBI spares skin toxicity. (A)** IHC staining for phosphorylated ERK of tail skin (10×) of mice receiving a single dose of the vehicle, or an equimolar dose of either COBI or TRX-COBI for 8 h, corresponding to Fig. 5 C. Scale bar: 20 µm. **(B)** Images of H&E (10×) showing the epidermal layer of tail skin in mice treated with the vehicle or equimolar doses of COBI or TRX-COBI for 20 d, corresponding to Fig. 5 D. Scale bar: 100 µm.

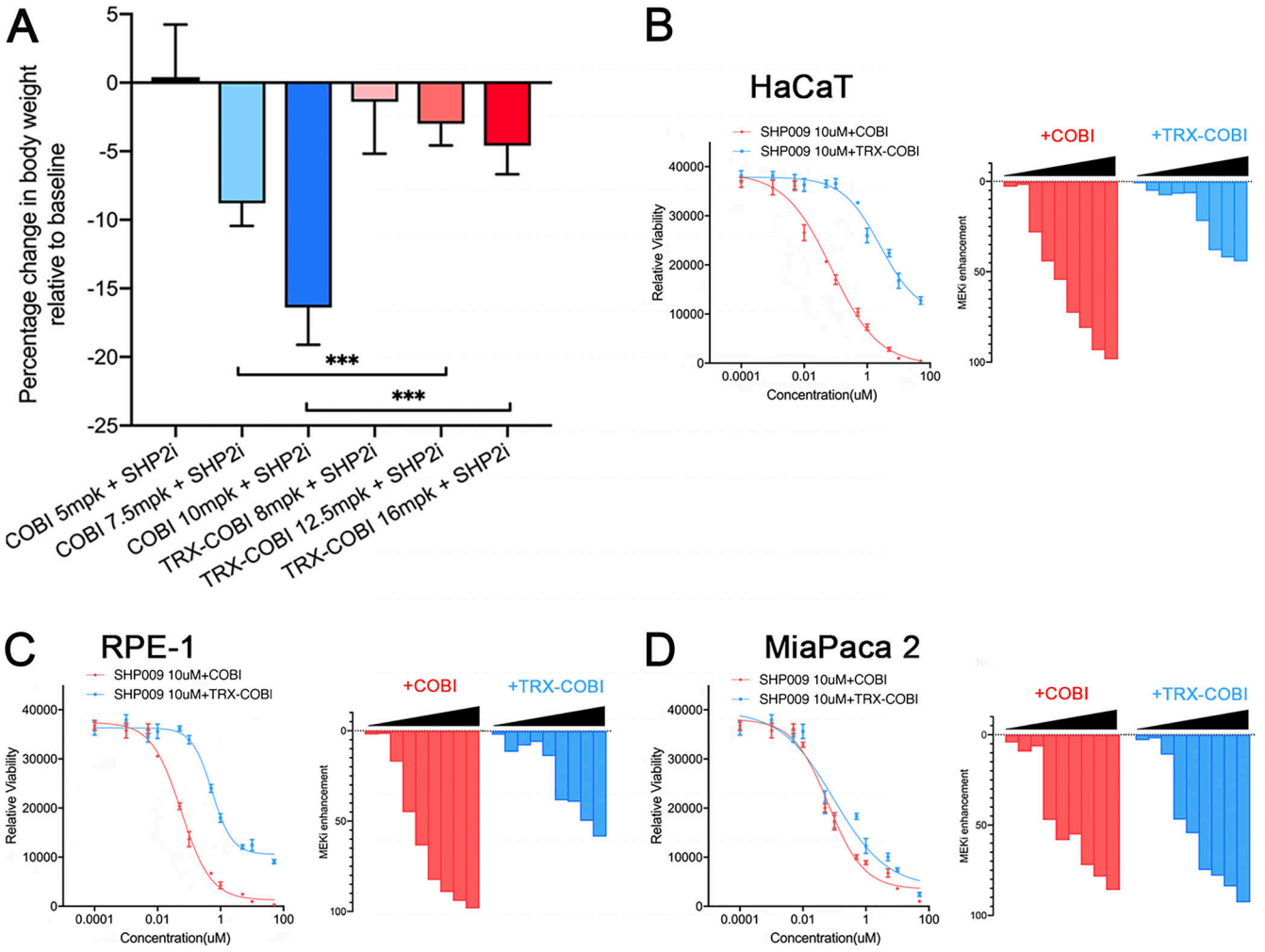

Figure S4. **FeADC-based MEK inhibition is tolerable in vivo and less toxic to normal cells. (A)** Mouse body weight changes normalized to the baseline after the treatment with indicated doses of COBI or TRX-COBI in combination with SHP009. Error bars represent mean ± SEM, *n* = 6 mice/group and analyzed by a two-sample *t*-test. ***, P < 0.001. **(B–D)** HaCaT, RPE-1, and MiaPaca2 cells were treated with increasing concentrations of COBI or TRX-COBI in the presence of 10 μM SHP009 for 72 h, and viability was determined. The enhancement of growth inhibition by the addition of COBI or TRX-COBI to SHP009 was determined by normalizing the viability after combination treatment to SHP009 for each dose point (0 = no effect; 100% = complete cell killing).

Provided online are Table S1, Table S2, Table S3, and Data S1. Table S1 lists stability of (1″*R*, 3″*R*)-TRX-COBI and (1″*S*, 3″*S*)-TRX-COBI conjugates in MLMs. Table S2 lists pharmacokinetic parameters for (1″*R*, 3″*R*)-TRX-COBI and (released) COBI following a single 15 mg/kg IP dose of (1″*R*, 3″*R*)-TRX-COBI to NSG mice. Table S3 lists key resources used in this study. Data S1 contains scans of NMR, HMRS spectra, and LCMS chromatograms.